

**Tsunami Decision Matrix for a  
strike-slip fault - The Gloria Fault in  
the NE Atlantic**

Anna Guglielmin

**Advisor:**

Prof. Alberto Armigliato

**Co-supervisors:**

Prof. Maria Ana Baptista

Dr. Rachid Omira



# Contents

<b>Contents</b>	<b>iii</b>
<b>Sommario</b>	<b>1</b>
<b>Abstract</b>	<b>3</b>
<b>1 The Gloria fault</b>	<b>9</b>
1.1 Definition of fault . . . . .	9
1.2 Classification of faults . . . . .	11
1.3 Gloria Fault's morphological description . . . . .	14
1.4 20 <sup>th</sup> century large earthquakes along the GF . . . . .	18
<b>2 Tsunami Alert Efficiency</b>	<b>21</b>
2.1 Decision matrix . . . . .	22
2.1.1 Tsunami Early Warning System and Threat Levels . . . . .	22
2.1.2 Unified Tsunami Message Approach and Spatial Ranges in the NEAM Region . . . . .	25

2.1.3	The Role and Significance of the Decision Matrix in Assessing Tsunami Threat Levels . . . . .	27
2.2	Problems of the application of the DM for the events along GF . . . .	28
<b>3</b>	<b>MIRONE and Shallow Water Equations</b>	<b>31</b>
3.1	Mirone in this case of study . . . . .	32
3.2	Preparation of the tsunami simulation . . . . .	33
3.3	Generation of tsunamis in the source area . . . . .	37
3.4	Tsunami Propagation and SWEs . . . . .	41
<b>4</b>	<b>Application of the DM to the GF</b>	<b>49</b>
4.1	25 November 1941 event . . . . .	50
4.1.1	1941 strike-slip event . . . . .	50
4.1.2	1941 dip-slip scenario . . . . .	53
4.2	26 May 1975 event . . . . .	60
4.2.1	1975 strike-slip event . . . . .	60
4.2.2	1975 dip-slip scenario . . . . .	63
4.3	1 January 1980 event . . . . .	68
4.3.1	1980 strike-slip event . . . . .	68
4.3.2	1980 dip-slip scenario . . . . .	69
4.4	A dip-slip event: 28 February 1969 . . . . .	76
4.4.1	1969 dip-slip event . . . . .	76
4.5	Effects of Epicenter Displacement on Tsunami Impact . . . . .	78

<i>CONTENTS</i>	v
4.6 Effects of Magnitude Modification on Tsunami Impact . . . . .	87
4.7 New proposal for the DM in the NE Atlantic . . . . .	95
<b>5 Conclusions</b>	<b>101</b>
<b>Bibliography</b>	<b>107</b>



# Sommario

Questa tesi investiga l'applicabilità della Matrice Decisionale per gli Tsunami del Nord Est Atlantico alle caratteristiche uniche della Faglia Gloria, una grande faglia trascorrente che si estende a Est delle Azzorre con il limite verso Gibilterra e segna il confine delle placche euroasiatica e nubiana. L'obiettivo di questa ricerca è valutare se la matrice decisionale esistente, progettata per valutare la minaccia di tsunami utilizzando parametri sismici di base, può essere efficacemente impiegata nel caso di questa specifica faglia. Per raggiungere questo obiettivo, viene effettuata un'analisi esaustiva utilizzando un insieme di terremoti rilevanti avvenuti nel XX secolo lungo questa faglia o nelle sue vicinanze, in particolare il terremoto del 25 novembre 1941 ( $M_s = 8.3$ ), il terremoto del 26 maggio 1975 ( $M_s = 7.9$ ), il 1° gennaio 1980 ( $M_s = 6.8$ ). L'unico evento con scorrimento verticale considerato è il terremoto del 28 febbraio 1969 ( $M_s = 7.9$ ), che si è verificato nella Piana Abissale Horseshoe nel Golfo di Cadice, mentre gli altri eventi sono tutti a scorrimento laterale. Questi eventi sismici, che hanno avuto epicentri situati nell'Atlantico NE lungo la Faglia Gloria o nelle sue vicinanze, serviranno come punti di riferimento chiave per la Matrice Decisionale. L'indagine comprende diversi aspetti, tra cui l'esame dei

record storici degli tsunami, le simulazioni numeriche degli tsunami e l'applicabilità della Matrice Decisionale. L'esame esaustivo delle passate occorrenze di tsunami fornisce preziose intuizioni sul comportamento e le caratteristiche dei tsunami causati da faglie trascorrenti. Studiando i dati storici, è possibile identificare schemi e tendenze per migliorare la matrice decisionale. I risultati di questa tesi contribuiscono a fornire importanti intuizioni nel campo delle previsioni in tempo reale degli tsunami, offrendo una comprensione più approfondita della pertinenza e degli eventuali adattamenti necessari per le matrici decisionali quando sono applicate a faglie trascorrenti come la Faglia Gloria.

# Abstract

This thesis investigates the applicability of the Northeast Atlantic tsunami Decision Matrix to the unique characteristics of the Gloria Fault, a large strike-slip fault of the Azores-Gibraltar fracture zone that marks the western plate boundary between the Eurasian and Nubian plates. The objective of this research is to assess whether the existing decision matrix, designed for evaluating tsunami threat using basic earthquake parameters, can be effectively employed in the case of this specific fault. To achieve this, a comprehensive analysis is performed using a set of relevant earthquakes occurred in the 20th century along this fault or in its vicinities, namely the 25 November 1941 ( $M_s = 8.3$ ), the 26th May 1975 earthquake ( $M_s = 7.9$ ), the 1 January 1980 ( $M_s = 6.8$ ). The only dip-slip event considered is the earthquake on February 28, 1969 ( $M_s = 7.9$ ), that took place in the Horseshoe Abyssal Plain in the Gulf of Cadiz, while all the other events are strike-slip events. These seismic events, which had epicenters located in the North East Atlantic, along the Gloria Fault, will serve as key benchmarks for the Decision Matrix. The investigation encompasses several aspects, including the examination of historical tsunami data records, tsunami numerical simulations and applicability of Decision Matrix. Exhaustive examination

of past tsunami occurrences provides valuable insights into the behavior and characteristics of tsunamis triggered by strike-slip faults. By studying the historical data, patterns and trends can be identified to enhance the decision matrix. The findings of this thesis contribute valuable insights to the field of tsunami real-time forecasting, offering a deeper understanding of the suitability and potential adaptations required for decision matrices when applied to strike-slip faults such as the Gloria Fault.

## **Outline of the thesis**

We present here the structure of the thesis.

### **Chapter 1: The Gloria Fault**

The first section, *Definition of fault*, will provide a clear definition of the Gloria Fault, explaining its geological characteristics and how it is formed. In section 1.2, *Classification of faults*, different types of faults will be discussed, including their distinguishing features and how they relate to the Gloria Fault. In section 1.3, *Gloria Fault's morphological description*, the physical characteristics of the Gloria Fault will be examined, such as its length, width, and vertical displacement. This section will provide a detailed understanding of the fault's morphology. Lastly, section 1.4, *20th-century large earthquakes along the Gloria Fault*, will focus on significant earthquakes that occurred along the Gloria Fault during the 20th century. The magnitude, impact, and notable features of these earthquakes will be discussed, shedding light on the seismic activity along the fault.

### **Chapter 2: Tsunami Alert Efficiency**

Section 2.1, *Decision matrix* will explore the decision matrix, which is a tool used to assess and communicate tsunami threat levels. It will discuss the components of the decision matrix and how it contributes to the efficiency of tsunami alerts. In subsection 2.1.1, *Tsunami Early Warning System and Threat Levels*, the role of the decision matrix within the broader context of the Tsunami Early Warning System will be explained. The different threat levels associated with tsunamis and their implications for warning systems will be discussed. In 2.1.2 *Unified Tsunami Message Approach and Spatial Ranges in the NEAM Region* will focus on the unified approach to tsunami messages, where all National Tsunami Warning Focal Points receive the same message. It will also discuss the spatial ranges defined in the NEAM region and how they are incorporated into the decision matrix. Then subsection 2.1.3, *The Role and Significance of the Decision Matrix in Assessing Tsunami Threat Levels*, will highlight the importance of the decision matrix in evaluating and categorizing tsunami threat levels. It will explain how the matrix aids in decision-making processes and the implementation of appropriate response measures. Section 2.2, *Problems of the application of the decision matrix for the events along the Gloria Fault*, will address the specific challenges and difficulties encountered when applying the decision matrix to tsunamis occurring along the Gloria Fault. It will discuss any unique considerations or factors that need to be taken into account when assessing threat levels for events associated with this fault.

### **Chapter 3: MIRONE and Shallow Water Equations**

Section 3.1, *Mirone in this case study*, will provide an overview of the application

of Mirone, a software tool, in the specific context of the study. It will discuss how Mirone is utilized and its significance in the analysis and visualization of tsunami data. Then 3.2, *Preparation of the tsunami simulation*, will cover the necessary steps involved in preparing the tsunami simulation. It will discuss the data and parameters required, as well as the methodologies employed to ensure an accurate and reliable simulation. In 3.3, *Generation of tsunamis in the source area*, the process of generating tsunamis in the source area will be explained. It will discuss the factors and mechanisms that contribute to the generation of tsunamis, as well as any specific considerations related to the study area. Finally, section 3.4 *Tsunami Propagation and Shallow Water Equations*, will delve into the concept of tsunami propagation and the use of Shallow Water Equations (SWEs) to model and analyze the behavior of tsunamis. It will explore the underlying principles of SWEs and their application in simulating tsunami propagation and the resulting wave characteristics.

#### **Chapter 4: Application of the DM to the GF**

In this chapter, the application of the Decision Matrix (DM) to specific events in the GF region is discussed. In section *25 November of 1941 event* the analysis of the 1941 strike-slip event is presented, focusing on its characteristics and implications for tsunami generation. Subsection 4.1.1 examines the details of the 1941 strike-slip event whereas in 4.1.2 the dip-slip scenario is discussed. Section *26 May of 1975 event* focuses on the analysis of the 1975 strike-slip event. Subsection 4.2.1 provides an overview of the 1975 strike-slip event and subsection 4.2.2 examines dip-slip scenario. The same is done for the 1980 event in section 4.3 *1 January of 1980 event* for the

strike-slip event (4.3.1) and dip-slip scenario (4.3.2) and for the 1969 event in section 4.4 *28 February of 1969* for the strike-slip event (4.4.1) and dip-slip scenario (4.4.2). Section 4.5 *Effects of Epicenter Relocation on Tsunami* investigates the effects of epicenter relocation on the resulting tsunami impact, considering its significance and implications, whereas 4.6 *Effects of Magnitude Modification on Tsunami Impact* does the same but for magnitude modification. Finally, section 4.7 *New proposal for the DM in the NE Atlantic* gives a new proposal for the Decision Matrix (DM) in the NE Atlantic. Conclusions are presented in Chapter 5.



# Chapter 1

## The Gloria fault

### 1.1 Definition of fault

At low temperatures and pressures, rock exhibits brittle behavior, making it susceptible to fracturing under high stress conditions. When this fracturing involves horizontal displacement, it is referred to as a *fault* (Turcotte and Schubert 2014). Surface faults can vary significantly in size, ranging from some centimeters to hundreds of kilometers. The

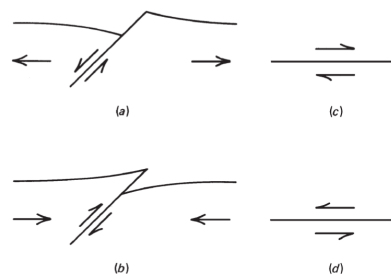


Figure 1.1: Cross sections of (a) a normal fault and (b) a thrust fault and top views of (c) right-lateral and (d) left-lateral strike-slip faults (Turcotte, D.L., Schubert, G., *Geodynamics*, (2014), p. 60).

occurrence of earthquakes is often associated with with displacements on many faults, where seismic activity is triggered when the stress acting on the fault exceeds a crit-

ical threshold, leading to a rupture. When a fault remains locked, elastic energy gradually builds up in the surrounding rocks due to displacements occurring at a distance. As the stress on the fault reaches a critical level, the fault slips, resulting in an earthquake. Throughout this process, the accumulated elastic energy in the adjacent rock is released and dissipated. Some of this energy is transformed into heat through friction along the fault plane, while the remaining energy is radiated as seismic energy. This phenomenon is commonly referred to as elastic rebound. Depending on fault locations, geometries, orientations and faulting style, faults can be classified in:

- *Thrust fault*, will occur if a region is in a state of compressional stress;
- *Normal fault*, will occur if a region is in a state of tensional stress;
- *Strike-slip fault*, will occur if a region is in a state of shear. If, to an observer standing on one side of the fault, the motion on the other side of the fault is to the left, the fault is a left-lateral strike-slip fault or sinistral strike-slip fault. Otherwise it is a right-lateral or dextral strike-slip fault.

Numerous earthquakes involve a combination of horizontal displacement resulting from strike-slip faulting and vertical displacement associated with either normal or thrust faulting, referred to as *transpression* or *transtension*, respectively.

## 1.2 Classification of faults

Since cavities cannot open at the depth of the earth, displacements on faults run parallel to the surface of the fault. For simplicity, the fault surface is assumed to be planar; in the real Earth, faults often occur on curved surfaces or on a series of surfaces that are offset from each other. As regards thrust faulting, this mechanism occurs when oceanic lithosphere is thrust beneath adjacent continental (or oceanic) lithosphere along an ocean trench. Thrust faults also play an important role in the compression of lithosphere during continental collisions. Idealized thrust faults are shown in Figure 1.2. Compressional stresses cause displacement along a fault plane inclined at an angle  $\beta$  to the horizontal. As a result of the faulting, horizontal compressional strain occurs.

Thrust faults can form in either of the two conjugate geometries shown in Figures 1.2 a and b. The elevated block is called the hanging wall and the lowered block is called the foot wall. The upward movement of the hanging wall is also called reverse faulting. Stresses in the horizontal and vertical directions are

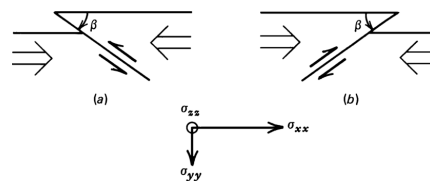


Figure 1.2: *Thrust faulting. Two conjugate thrust faults with dip angles  $\beta$  are shown in (a) and (b). The principal stresses illustrated in (c) are all compressional with magnitudes  $\sigma_{xx} > \sigma_{zz} > \sigma_{yy}$  (Turcotte, D.L., Schubert, G., *Geodynamics*, (2014), p. 390).*

assumed to be the principal stresses. The vertical stress component  $\sigma_{yy}$  is the lithostatic pressure. The vertical deviatoric stress  $\Delta\sigma_{yy}$  is null, while a compressional deviatoric stress  $\Delta\sigma_{xx}$  is applied in the x direction. The horizontal compressional

stress,  $\sigma_{xx} = \rho gy + \Delta\sigma_{xx}$ , therefore exceeds the vertical lithostatic stress  $\sigma_{xx} > \sigma_{yy}$ .

For the fault geometry shown in Figure 1.2 it has been assumed that there is no

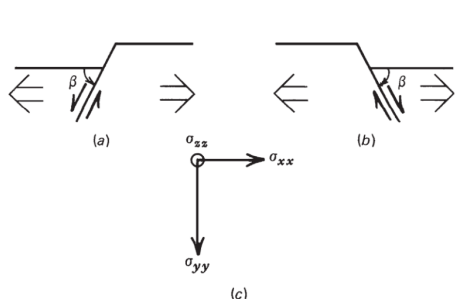


Figure 1.3: *Normal faulting.* Two conjugate normal faults with angle of dip  $\beta$  are shown in (a) and (b). The principal stresses illustrated in (c) have magnitudes related by  $\sigma_{yy} > \sigma_{zz} > \sigma_{xx}$  (Turcotte, D.L., Schubert, G., *Geodynamics*, (2014), p. 391).

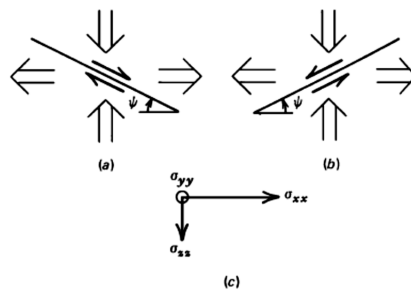


Figure 1.4: *Strike slip faulting.* Two conjugate strike slip faults inclined at an angle  $\psi$  to the direction of the principal stress  $\sigma_{xx}$  are shown in (a) and (b). The principal stresses illustrated in (c) are related by  $\sigma_{zz} > \sigma_{yy} > \sigma_{xx}$  (Turcotte, D.L., Schubert, G., *Geodynamics*, (2014), p. 391).

strain in the z direction. In this situation of plane strain, using

$$\sigma_3 = \nu(\sigma_1 + \sigma_2) \quad (1.1)$$

where  $\sigma_i$  are the principal stress components, that relates the deviatoric stress component  $\Delta\sigma_{zz}$  to  $\Delta\sigma_{xx}$  by  $\Delta\sigma_{zz} = \nu\Delta\sigma_{xx}$  meaning that the deviatoric stress in the z direction is also compressional, but its magnitude is a factor of  $\nu$  less than the deviatoric applied stress, where  $\nu$  is a property of the material known as the Poisson's ratio. Therefore the horizontal compressional stress,

$$\sigma_{zz} = \rho gy + \Delta\sigma_{zz} = \rho gy + \nu\Delta\sigma_{xx} \quad (1.2)$$

is larger than the vertical stress  $\sigma_{yy}$ , but it is smaller than the horizontal stress  $\sigma_{xx}$ . Thrust faults satisfy the condition  $\sigma_{xx} > \sigma_{zz} > \sigma_{yy}$ . The vertical stress is the least compressive stress. Just as thrust faulting accommodates horizontal compressional strain, normal faults accommodate horizontal extensional stresses. Normal faults occur on the flanks of oceanic ridges where new lithosphere is formed. Normal faults also occur in continental rift valleys where lithosphere is stretched. Applied tensional stresses can produce normal faults in either of the two ways shown in Figure 1.3. The displacements on the fault planes dipping at an angle  $\beta$  to the horizontal lead to horizontal extensional strain. Normal faulting is associated with a state of stress in which the vertical component of stress is the lithostatic pressure

$$\sigma_{yy} = \rho gy \quad (1.3)$$

and the applied deviatoric horizontal stress is tensional (negative). The horizontal stress, is therefore smaller than the vertical stress,  $\sigma_{yy} > \sigma_{xx}$ . The plane strain assumption is again appropriate to the situation, and equation 1.2 is applicable. Consequently, the deviatoric stress in the  $z$  direction is also tensional, but its magnitude is a factor of  $\nu$  smaller than the deviatoric applied stress. Normal faults satisfy the condition  $\sigma_{yy} > \sigma_{zz} > \sigma_{xx}$  where the vertical stress is the maximum compressive stress. Both thrust faults and normal faults are also known as dip-slip faults because the displacement along the fault takes place mainly along the dipping direction. A strike-slip fault is a fault along which the displacement is strictly horizontal. Consequently there is no strain in the  $y$  direction. The situation is one of plane strain with

the non-zero strain components confined to the horizontal plane. Vertical views of two conjugate strike-slip faults are shown in Figure 1.4. The fault planes make an angle  $\psi$  with respect to the direction of the principal stress  $\sigma_{xx}$ . The fault illustrated in Figure 1.4 a is right lateral and 1.4 b left lateral. The state of stress in strike-slip faulting consists of a vertical lithostatic stress  $\sigma_{yy} = \rho gy$  and horizontal deviatoric principal stresses that are compressional in one direction and tensional in the other. The case shown in Figure 1.4 has  $\sigma_{xx} < 0$  and  $\sigma_{zz} > 0$  but can be the opposite. One horizontal stress will thus be larger than  $\sigma_{yy}$  while the other will be smaller. Using the previous equations, it results  $\sigma_{zz} > \sigma_{yy} > \sigma_{xx}$  and  $\sigma_{xx} > \sigma_{yy} > \sigma_{zz}$ . For strike-slip faulting, the vertical stress is always the intermediate stress. The displacement on an actual fault is almost always a combination of strike-slip and dip-slip motion. However, one type of motion usually dominates. A combination of strike-slip and thrust faulting is known as transpression. A combination of strike-slip and normal faulting is known as transtension.

### 1.3 Gloria Fault's morphological description

The Azores-Gibraltar fracture zone (AGFZ) is the western boundary between the Eurasian and Nubian plates (Omira, Neres, Batista, 2019). It extends from the Mid-Atlantic Ridge located in the Azores in the west to the Strait of Gibraltar in the east. The AGFZ traverses three distinct morphotectonic domains, namely the Azores triple junction zone, the Gloria Fault (GF), and the southwest Iberian Margin (SWIM), which experience different kinematic and stress regimes. The GF is

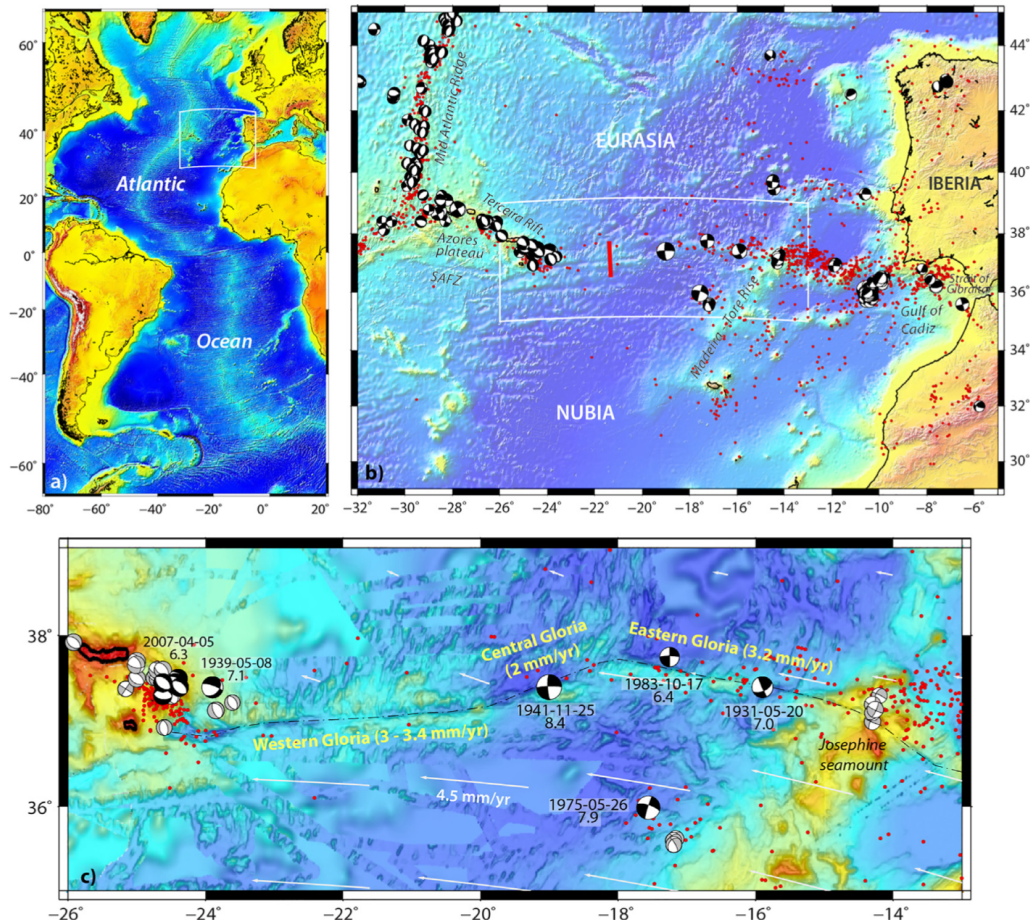


Figure 1.5: (A) Location of the study area in the Atlantic Ocean. (B) The Azores-Gibraltar fracture zone (AGFZ) and its regional context. Red dots are epicenters of  $M > 4$  earthquakes from the International Seismological Center (ISC) for the period 1970–2017. Focal mechanisms from the database compiled by Custódio et al. (2016) ( $M > 5$ ). Red line locates the seismic refraction and multichannel seismic reflection profiles by Batista et al. (2017). SAFZ: South Azores fracture zone. (C) The Gloria Fault. Red dots:  $M > 4$  epicenters. Focal mechanisms (Custódio et al., 2016 database) for earthquakes  $M > 5$  (in gray) and  $M > 6$  (in black, labels indicate date and magnitude). White arrows: vectors from the relative NU-EU velocity field as modeled by the neotectonic model of Neres et al. (2016). Yellow labels: Gloria Fault segments and respective slip rates as inferred by Neres et al. (2016) (note that the model allows for fault slip and continuum strain rate).

a significant transform segment of the AGFZ and constitutes its central domain. It encompasses a less well-known segment of about 900 km, which exhibits anomalous deep structures that have been studied by scientists. The GF derives its name from the Geological LOng-Range Inclined Asdic (GLORIA) sonar, which was the first side scan sonar used to map large oceanic areas. The GF comprises three primary segments, which combine to form a composite structure:

- Western Gloria, located between 24°W and 19°30' W, it strikes parallel to the average direction of NU-EU motion, so this is essentially accommodated by strike-slip faulting;
- Central Gloria, located between 19°30' W and 18°W, it jogs to ENE-WSW, slightly oblique to the kinematic vectors and likely prone to some dextral compressive strain;
- Eastern Gloria, located from 18°W to 14°30' W, it strikes again parallel to the NU-EU motion.

Morphologically, the GF is a depression that is approximately 20 km wide and has a vertical offset of over 1 km, with elongated basins between ridges that are also elongated in an E-W direction (as shown in Figure 1.5 c). Recently, Batista et al. (2017) investigated the crustal structure of the GF using N-S seismic profiles. They found that the basins above the GF have a maximum depth of 1 km, and are bounded by steep fault planes that dip at an angle of 75 degrees. The authors also observed differences in bulk sedimentation and tectonic deformation between the north and

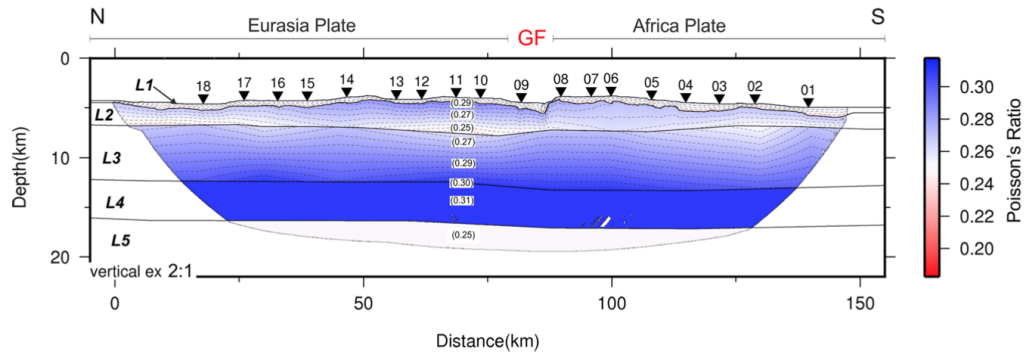


Figure 1.6: Poisson's ratio model obtained from  $V_p$  and  $V_s$  models; L1 to L5—modeled layers; contours are spaced 0.005. (Baptista L. et al., 2017)

south sides of the GF, which mark the Eurasian and Nubian plates. The northern side is characterized by minor tectonic movements and a sequence of north-south trending ridges that deflect to NNE-SSW as we move eastward. In contrast, the ridges in the southern side of the GF are not as pronounced and are responsible for most of the deformation associated with the GF's strike-slip movement. The authors also presented a five-layer  $V_p$  velocity model (L1-L5 in Figure 1.6) based on wide-angle data analysis.

- L1 comprises both pelagic sediments and basaltic flows or volcanic sedimentary complex;
- L2 (3 km thick) presents a basaltic composition normally referred to as oceanic upper crust;
- L3 (5 km thick) is in agreement with a gabbroic composition normally referred to as oceanic lower crust;
- L4 (4 km thick) was interpreted as partial serpentinization of the upper litho-

spheric mantle;

- L5 corresponds to upper mantle.

Batista et al. (2017) conducted an experiment that revealed the thickness of the crust in the Gloria Fault (GF) strike and the regions north and south of it. The thickness of the crust in the GF strike was found to be approximately 8 km, while the thickness toward the north and south was approximately 7 km. Despite being considered a localized transform plate boundary, the seismicity record challenges this assumption. Seismic activity is more significant in the Azores and southwest Iberian Margin domains but less along the Gloria domain. The eastern Gloria segment has the most seismic activity, while the western Gloria segment has almost no seismic event. In addition, the recorded earthquakes' epicenters do not follow the Gloria trend but seem to be spread around it, possibly due to inaccurate localization of events resulting from the long distance to the seismic networks and low azimuthal coverage of the oceanic area.

#### 1.4 20<sup>th</sup> century large earthquakes along the GF

The Gloria area has been the origin of different large earthquakes (with a magnitude higher than 7) in the 20<sup>th</sup> century which have been followed by small or moderate tsunamis. In this thesis three large instrumental strike-slip events ( $M_w = 8.3$ , November 25, 1941,  $M_w = 7.9$ , May 26, 1975 and  $M_w = 6.8$ , January 1, 1980) that have been recorded within the Gloria domain, all located very close to its morphological structure, and a dip-slip one, ( $M_w = 7.9$ , February 28, 1969) which occurred

specifically in the vicinity of the Iberian Peninsula, outside the Gloria Fault, will be analyzed. This suggests that large events/ruptures would preferably localize along the main structure, irrespective of a possible more spread location of the small events (Omira et al. 2019). They can be summarized by their main characteristics:

- The  $M_w = 8.3$ , November 25, 1941, occurred in the central segment of the GF and was the largest strike-slip earthquake recorded until the  $M_w = 8.6$  Sumatra earthquake in 2012. This caused a tsunami that was recorded by stations in Portugal, Morocco, Madeira, and Azores islands, with a peak wave height of 0.7 m in Ponta Delgada. The significant magnitude of the earthquake suggests a potential long rupture propagating across multiple segments, possibly extending to the western Gloria domain. The occurrence of such a large rupture has been considered as a possible explanation for the low seismicity observed along the GF, implying a locked and accumulating stress condition for a future major event.
- The earthquake event on February 28, 1969, with a magnitude of  $M_w = 7.9$ , occurred off the coast of Portugal. It is the only dip-slip event considered in this thesis, characterized by a thrust focal mechanism.
- The  $M_w = 7.9$ , May 26, 1975, occurred approximately 100 km south of the Gloria area. It resulted in a small tsunami, which was recorded by the Portuguese, Spanish, and Moroccan tide-gauge networks.
- The  $M_w = 6.8$ , January 1, 1980, with its epicentre between Terceira and

San Jorge Islands. This earthquake caused damages in those islands but no significant tsunami was recorded.

The spatial distribution of these significant events implies that the Gloria region does not solely represent a single active plate boundary structure. Instead, it appears to encompass a broader plate boundary zone characterized by distributed transform motion across multiple fracture zones.

## Chapter 2

# Tsunami Alert Efficiency

Following the catastrophic tsunamis of the 21st century, namely the 26 December 2004 Sumatra  $M_w = 9.1$  earthquake, which resulted in the loss of a quarter of a million lives, and the 11 March 2011 Tohoku-Oki  $M_w = 9.0$  earthquake, which claimed the lives of around 18,500 individuals, there was a pressing need to coordinate tsunami warning efforts and minimize risk. As a response, the third United Nations World Conference on Disaster Risk Reduction convened on 18 March 2015 in Sendai, Japan, and adopted the "Sendai Framework for Disaster Risk Reduction 2015–2030" (Yahav, Salamon, 2022). This framework seeks to achieve the following objectives:

- Enhance the understanding of disaster risk;
- Strengthen disaster risk governance for effective management of disasters;
- Invest in disaster risk reduction for building resilience;
- Enhance disaster preparedness for effective responses, and to "Build Back Bet-

ter" during recovery, rehabilitation, and reconstruction efforts;

- Reduce disaster losses of lives and assets worldwide.

The primary objective of tsunami alert systems is to facilitate timely, precise, and reliable management of tsunami warning communications, encompassing the entire process from detecting a potential tsunamigenic earthquake to disseminating relevant information to individuals residing in vulnerable areas. The goal is to ensure that all individuals at risk receive prompt and accurate warnings, allowing them to take appropriate actions to safeguard their lives.

## 2.1 Decision matrix

### 2.1.1 Tsunami Early Warning System and Threat Levels

The effectiveness of a Tsunami Early Warning System (TEWS) hinges on its ability to deliver timely and accurate warnings to all regions susceptible to tsunami impact. A crucial aspect of this effectiveness lies in the rapid identification of coastal areas at risk. Therefore, all components of the TEWS must operate with high efficiency within a matter of minutes. This becomes particularly critical in regions with near-shore tsunamigenic sources, such as Europe and the Mediterranean Sea. To address this challenge, the Intergovernmental Coordination Group for the Tsunami Early Warning and Mitigation System in the North-Eastern Atlantic, the Mediterranean, and connected seas (ICG/NEAMTWS) has proposed the adoption of a decision-making tool known as the "Decision Matrix" (DM). The DM focuses specifically on

tsunamis triggered by earthquakes and relies on two key parameters: the magnitude of the earthquake and the location of its epicenter. By utilizing this matrix, relevant authorities can make informed decisions regarding the appropriate response measures based on the initial characteristics of the tsunami event. Ideally, a tsunami alert message should contain three essential pieces of information required by emergency management agencies, following the Common Alerting Protocol (CAP) notation: urgency, severity, and certainty (Tab. 2.1). Additionally, the affected area should be clearly indicated in the message, listing the countries that are at risk. By incorporating these elements, the initial lines of a tsunami message would promptly convey the fundamental information to the recipient, while further details of the threat evaluation would be provided in the subsequent sections of the message. To ensure effective communication, the North-Eastern Atlantic, Mediterranean, and connected seas Tsunami Information Centre (NEAMTIC) proposes two levels of threat for each information instance: urgency, severity, and certainty. These levels enable a more precise assessment of the imminent danger and help emergency management agencies in making informed decisions and implementing appropriate response measures.

	Level I (High)	Level II (Low)
Urgency	Tsunami to arrive in less than 2 <sup>1</sup> hours	Tsunami to arrive in more than 2 <sup>1</sup> hours
Severity	Tsunami wave height greater than 0.5m and/or tsunami run-up greater than 1m	Tsunami wave height less than 0.5m and/or tsunami run-up less than 1m
Certainty	Tsunami confirmed by sea-level measurements	Tsunami not yet confirmed by sea-level measurements, information based on seismic parameters only

Table 2.1: Levels of Tsunami Alert Parameters

And for each level suggests the use of the following keywords to classify them:

	Level definition for the 3 parameters	
	Level I (high)	Level II (low)
Urgency	Immediate	More than 2 hours
<i>Severity</i> <sup>1</sup>	Watch	Advisory
Certainty	Confirmed	Not yet confirmed

Table 2.2: Definition of levels for the tsunami alert parameters.

In the table above, two levels are defined for each of the three parameters: urgency, severity, and certainty. Level I (high) indicates the more critical or immediate condition, while Level II (low) represents a less severe or time-extended situation. The urgency level distinguishes between an immediate response and a timeframe of more than two hours. The severity level is categorized as a "Watch" for Level I and an "Advisory" for Level II. The certainty level specifies whether the tsunami has been confirmed or is yet to be confirmed. After an earthquake event, the dissemination of information through the Tsunami Early Warning System involves three distinct message types, each indicating a different level of severity regarding the potential impact of the tsunami (as detailed in Tab. 2.3). The initial message type, referred to as the "information bulletin," serves to notify the occurrence of a significant earthquake (specifically, with a moment magnitude  $M_w \geq 5.5$ ). Although the earthquake may have triggered a tsunami, its expected magnitude is deemed insufficient (with wave heights below 20 cm) to cause any significant damage within the specified distance range. The subsequent message type, termed the "advisory bulletin," represents the second tier of the NEAMTWS matrix's tsunami alert system. It indicates an an-

<sup>1</sup>Number to be agreed upon the Intergovernmental Coordination Group, ICG

anticipated impact along the coastline, with the potential for tsunami waves reaching heights of 0.5 m in near-shore areas such as harbors and coastal channels. These areas may experience strong currents and the formation of bores. Additionally, onshore regions might witness run-up heights of up to 1 m, which could result in localized inundation of certain low-lying flat beaches. Finally, the highest level of alert is the "tsunami watch," issued when significant to catastrophic damage is expected. This level of alert signifies the potential for loss of life, as tsunami waves exceed 0.5 m in height, and extensive coastal inundation becomes a concern. In such cases, run-up heights could surpass 1 m, posing a substantial threat to coastal regions (Tinti, 2012).

Message Type	Tsunami Wave	Effects on the Coast
Tsunami Watch	Tsunami wave height greater than 0.5 m and/or tsunami run-up greater than 1 m	Coastal inundation
Tsunami Advisory	Tsunami wave height larger than 0.2 m and/or run-up less than 1 m	Currents, bores, recession, damage in harbours, small inundation on beaches
Tsunami Information		No tsunami threat

Table 2.3: Tsunami Message Types as Defined by the ICG/NEAMTWS in the 2010 OUG

### 2.1.2 Unified Tsunami Message Approach and Spatial Ranges in the NEAM Region

In the NEAM (North-East Atlantic, Mediterranean, and connected seas) region, the basin structure gives rise to varying levels of tsunami threats, making it impractical to assign the same threat level to all countries. However, sending different messages

to different countries for the same tsunami event can lead to confusion. To address this, it has been proposed a unified approach where all National Tsunami Warning Focal Points (TWFP) in the NEAM region receive the same tsunami message. This unified message will incorporate multiple types of messages within its body, including tsunami watch, tsunami advisory, and tsunami information. To ensure clarity, the header section of the tsunami message will present a sequence of pairs consisting of message type and affected area. These pairs will be arranged in decreasing order of threat level. The overall type of the composed message will correspond to the highest level of tsunami threat present in the region. Consequently, the message will indicate that a certain coastal area in the NEAM region is susceptible to that specific type of tsunami threat. Hence, a Tsunami Watch message will encompass Tsunami Advisory and Tsunami Information types of messages within it. Similarly, a Tsunami Advisory message will include a Tsunami Information type of message. The specific areas affected by each level of tsunami threat are defined in the Decision Matrices established and agreed upon by the Intergovernmental Coordination Group for the Tsunami Early Warning and Mitigation System in the North-Eastern Atlantic, the Mediterranean, and connected seas (ICG/NEAMTWS). These matrices delineate the spatial ranges of tsunamis and the corresponding areas under threat. In particular Tab. 2.4 presents the three spatial ranges of tsunamis: Local, Regional, and Basin. The corresponding distances for each range are specified for both the Mediterranean and NE Atlantic regions.

<b>Tsunami Range</b>	<b>Mediterranean</b>	<b>NE Atlantic</b>
Local	< 100 km	< 100 km
Regional	100 km to 400 km	100 km to 1000 km
Basin	> 400 km	> 1000 km

Table 2.4: Tsunami Spatial Ranges.

### 2.1.3 The Role and Significance of the Decision Matrix in Assessing Tsunami Threat Levels

The Decision Matrix plays a vital role in assessing and communicating the threat level associated with tsunamis generated by earthquakes and, as said before, focuses on two essential parameters: the magnitude of the earthquake and the location of its epicenter, which enable the categorization of tsunamis into distinct threat levels. These threat levels serve as valuable indicators for emergency management agencies and relevant authorities, aiding in the prompt determination of appropriate response measures and the issuance of suitable warnings to the coastal regions at risk. The magnitude of the earthquake provides insights into the energy released during the seismic event. It helps in assessing the potential size and strength of the resulting tsunami waves. Additionally, the location of the epicenter allows for the evaluation of the proximity of the tsunami source to the vulnerable coastal areas, providing valuable information regarding the potential impact on these regions. Through the utilization of the DM, emergency management agencies can efficiently prioritize their response efforts based on the threat levels identified. This structured approach ensures that resources are allocated appropriately, enabling swift and effective actions to mitigate the potential impact of tsunamis. Overall, the Decision Matrix serves as

an essential tool in the comprehensive assessment of tsunamis, enhancing the early warning and preparedness systems in the North-Eastern Atlantic, the Mediterranean, and connected seas region. In Table 2.5 the last DM for the NE Atlantic proposed is shown.

Decision Matrix for the NE Atlantic						
Depth (km)	Epicentre Location	Earthquake Magnitude (Mw)	Tsunami Potential	Type of tsunami message		
				Local	Regional	Ocean-wide
<100km	Offshore or close to the coast ( $\leq 40$ km Inland)	$>5.5$ and $\leq 7.0$	Weak potential for a destructive local Tsunami	Advisory	Information	Information
		$>7.0$ and $\leq 7.5$	Potential for a destructive local Tsunami	Watch	Advisory	Information
	Offshore or close to the coast ( $\leq 100$ km Inland)	$>7.5$ and $\leq 7.9$	Potential for a destructive regional Tsunami	Watch	Watch	Advisory
		$>7.9$	Potential for a Destructive ocean-Wide tsunami	Watch	Watch	Watch
$\geq 100$ km	Offshore or Inland ( $\leq 100$ km Inland)	$>5.5$	No tsunami potential	Information	Information	Information

Table 2.5: Decision Matrix for the North-East Atlantic Ocean. Version proposed by the ICG/NEAMTWS in November 2011. “Loc”, “Reg” and “BW” stand for “Local”, “Regional” and “Basin-Wide” tsunami. “A”, “I” and “W” stand respectively for “Advisory”, “Information” and “Watch” and specify the type of bulletin.

## 2.2 Problems of the application of the DM for the events along GF

The application of a decision matrix for tsunami events to the Gloria Fault (a strike-slip fault) can pose several challenges and limitations. Some of the potential problems

## 2.2. PROBLEMS OF THE APPLICATION OF THE DM FOR THE EVENTS ALONG GF 29

include:

1. Lack of historical tsunami data: The Gloria Fault may not have a well-documented history of generating tsunamis. Since most decision matrices rely on historical data to assess the potential impact of a tsunami, the absence of such data for the Gloria Fault can limit the accuracy and reliability of the matrix's results.
2. Uncertainty in fault behavior: The behavior of the Gloria Fault in relation to generating tsunamis may not be well understood. The fault's predominant slip motion being strike-slip can potentially reduce the vertical displacement of the seafloor, which is a crucial factor in generating significant tsunamis. This uncertainty can affect the applicability of the decision matrix, as it may not account for the specific characteristics of strike-slip faults.
3. Incomplete understanding of local tsunami sources: Tsunamis can be generated by various sources, including earthquakes, landslides, and volcanic activity. While the Gloria Fault is primarily known for its strike-slip motion, there might be other local sources of tsunamis in the region that are not adequately considered in the decision matrix. Neglecting these additional sources can lead to incomplete risk assessment.
4. Difficulty in predicting tsunami characteristics: Tsunami generation, propagation, and inundation are complex phenomena influenced by several factors such as fault geometry, bathymetry, and coastal topography. The application of a decision matrix assumes accurate prediction of these characteristics, which can

be challenging for a specific fault like the Gloria Fault due to limited data and uncertainties in the associated parameters.

5. Context-specific considerations: Decision matrices for tsunamis are often designed based on general characteristics of subduction zone earthquakes and associated tsunamis. The Gloria Fault, being a strike-slip fault, may require specific modifications or adjustments to the decision matrix to account for the unique characteristics and potential differences in tsunami generation and propagation.

Overall, applying a decision matrix designed for tsunamis to the Gloria Fault, a strike-slip fault, requires careful consideration of these limitations and potential discrepancies. It is crucial to incorporate the specific characteristics and uncertainties associated with the fault to ensure accurate and reliable risk assessment.

## Chapter 3

# MIRONE and Shallow Water

## Equations

Mirone (Luis, 2007) is a widely used open-source software package that provides a versatile set of tools for visualizing, manipulating and analyzing various types of grid data, such as bathymetric and topographic data, satellite imagery, and geophysical data. It also includes modules for tsunami modeling, which can be used to simulate the propagation of tsunamis caused by earthquakes, landslides, or other sources. The tsunami modeling module in Mirone implements the finite-difference method and can be used to simulate tsunamis on a global or regional scale. The software allows the user to specify the source characteristics, including the location, magnitude, and orientation of the earthquake, as well as the bathymetry and topography of the affected region. The resulting tsunami waveforms can be visualized in various ways, including as time series, travel-time maps, and inundation maps, which can be used

to assess the potential impact of tsunamis on coastal communities and infrastructure. Mirone is a powerful tool that enables researchers and practitioners to explore and analyze grid data in a user-friendly and efficient way, and to simulate and visualize the effects of tsunamis in different scenarios.

### 3.1 Mirone in this case of study

In the case of study of the 20th century events along the Gloria Fault the package was used considering the focal mechanisms of the tsunamis in exam. In particular the procedure followed was:

- Select the event to model and add the location of the stations in which there are records;
- Find in the literature the values of magnitude and the focal mechanisms that generated the event;
- Draw the fault in the spatial grid and add the values of interest;
- Compute the coseismic deformation of the sea bottom caused by the earthquake with the Okada (1985) equations;
- Consider that the water is incompressible and assume that the initial sea surface elevation (at time  $t=0$  s) mimic this ocean bottom deformation;
- Model the event;
- Compare the modeled values with recorded values (if present).

## 3.2 Preparation of the tsunami simulation

For the determination of the single scenarios for DTHA (Deterministic Tsunami Hazard Assessment) and computation of tsunami propagation and impact for each scenario the benchmarked numerical code NSWING (Non-linear Shallow Water Model with Nested Grids) (Miranda et al., 2014) has been employed. In order to conduct a numerical modeling of a tsunami, various information and data are required. The life of a tsunami can be categorized into three distinct stages: Generation, Propagation, and Inundation. Similarly, numerical simulations of tsunamis follow the same sequence. The investigation begins by identifying the specific regions responsible for generating tsunamis and collecting data pertaining to the Typical Faults (TFs), which represent an average geometry for the finite-fault input in the tsunami simulation (Lorito, 2008). Subsequently, these parameters are utilized to compute the initial sea surface elevation, which serves as the initial condition for initializing the numerical model. The geographical region under investigation must be reconstructed as a Digital Elevation Model (DEM), encompassing detailed information regarding the bathymetric characteristics. To accurately represent the coastal regions, it is essential to acquire high-resolution DEMs in close proximity to the coast. Depending on the spatial extent between the tsunami source and the study area, a system of interconnected nested grids is employed to ensure an appropriate resolution within the study area. This paragraph provides a comprehensive description of these stages, elucidating the methodology employed in this thesis. The following steps are carried out to launch the NSWING model: (i) Computation of the initial condition, (ii)

Preparation of the DEM covering the oceanic path between the source area and the study area, (iii) Implementation the DEM in a system of nested grids, (iv) Choice of the physical quantities to describe the tsunami impact in the study area: run up, flow depth, maximum inundation distance, and launch the simulation.

- (i) Computation of the initial condition: Firstly, it is necessary to delineate the seismic conditions encompassing the fault parameters responsible for inducing tsunamis. This entails an understanding of the geographical regions susceptible to tsunamigenic earthquakes and their associated Typical Faults (TFs), as documented in the works of Miranda et al. (2008) and Omira et al. (2009). Comprehensive analysis of all potential earthquake sources is vital, necessitating the utilization of parameters derived from the most recent publications. The initial condition is calculated using the model introduced by Okada (1985) integrated within the Mirone suite. The designated fault is delineated on the parent grid. The parent grid used in this work spans from  $-30.2542^\circ$  W to  $-3.3358^\circ$  W longitude and from  $30.3601^\circ$  N to  $50.82970^\circ$  N latitude, encompassing all areas prone to tsunamigenic events, including the open ocean and the study area. The outcome of the initial condition computation is saved as a finite grid file with identical spatial extents as the parent grid. Once the initial conditions for all Typical Faults (TFs) are computed, they are stored in a designated folder to be utilized in the subsequent launch of the NSWING model. Further elaboration on the theoretical foundation underpinning the modeling of the initial condition can be found in a qualitative manner in section 3.3.

- (ii) Definition and launching of the tsunami simulation: The successful execution of a tsunami simulation necessitates the appropriate preparation of NSWING operational files and the files mentioned in the preceding section (i). To facilitate this, an executable batch file must be modified to enable NSWING to access the previously prepared files. Moreover, additional operators are incorporated to calculate desired information during the simulation. In this particular study, a list in DAT format containing geographical coordinates corresponding to the virtual tide gauge positions has been prepared. NSWING reads this file and records the free surface elevation at these designated points at specific time intervals. This enables subsequent waveform analysis and facilitates comparisons with existing records. The process of simulating tsunami propagation and inundation is detailed in the following subsections, outlining the computational procedures involved in these aspects of the study.

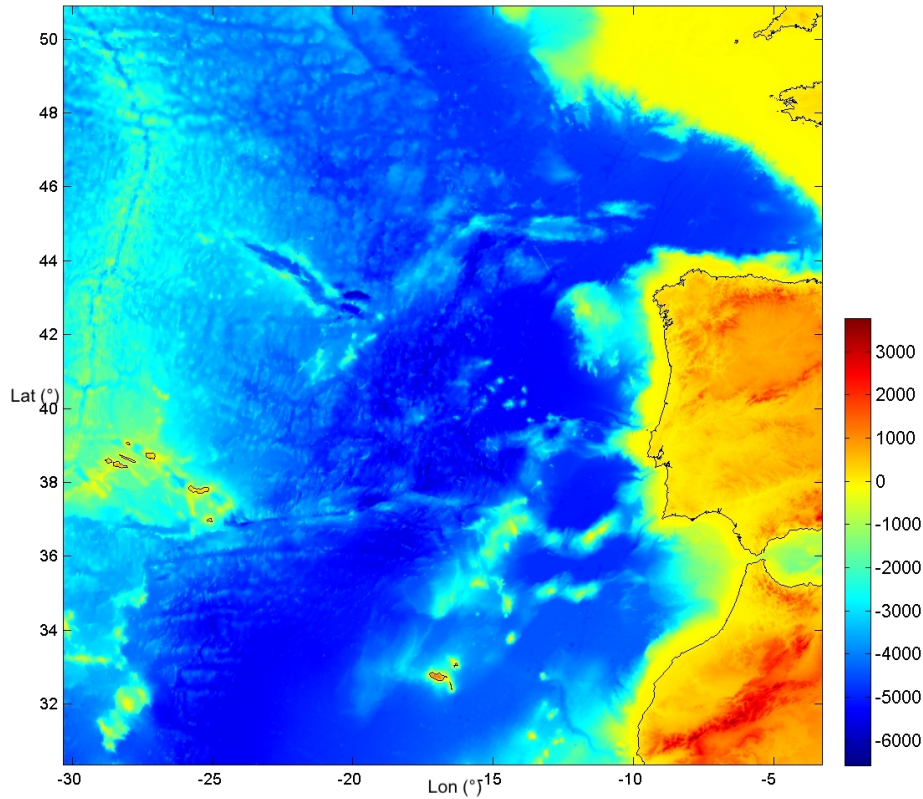


Figure 3.1: Parent grid used in this work. Colorbar indicates the surface elevation (m).

The DTHA method allows for the estimation of various physical quantities associated with tsunamis, including wave height, flow depth, drawback, inundation extent, velocities, and maximum current speed. These quantities are essential for creating scenario maps, conducting vulnerability studies, and establishing evacuation measures. In the case of assessing the vulnerability of buildings or coastal structures, mapping the maximum current speed becomes particularly important. Tsunami travel time maps illustrate the arrival times of the initial waves in the study area. In this study virtual tide gauges are strategically placed to analyze the waveforms observed at specific locations. Key information such as wave polarity, period recorded

by the tide gauges, and the time it takes for the waves to dissipate can be obtained from these analyses, but are not reported in this study. However, the primary focus was on studying the maximum wave height for various scenarios. This information was crucial for the development of a new Decision Matrix pertaining to the area under investigation.

### 3.3 Generation of tsunamis in the source area

Tsunamis can be generated by various natural events such as submarine earthquakes, landslides, volcanic eruptions, or meteorite impacts. In the context of this thesis, the focus is specifically on investigating the tsunami real-time forecasting associated with earthquakes. Earthquake-induced tsunamis typically occur at or near tectonic faults, particularly along plate boundaries. As already discussed in Chapter 1, there are three main types of faults that can be distinguished: strike-slip or transform faults, normal faults, and thrust or reverse faults. Strike-slip faults primarily involve horizontal movement and usually do not result in significant tsunami generation. However, in certain cases, the rupture mechanism along these faults may induce a significant vertical component, which can potentially trigger a tsunami. This happens in particular when the strike-slip fault ruptures in correspondence with relevant topo-bathymetric gradients (Tanioka and Satake, 1996). Normal faults and reverse faults, on the other hand, involve vertical seabed motion. These types of faults are capable of lifting or lowering the water column above, thus initiating motion at the sea surface. In some instances, reverse faults may also include horizontal components

contributing to the overall motion (details in Chapter 1). The initial deformation of the sea surface is calculated using analytical formulas based on the work of Mansinha and Smylie (1971), as synthesized in Okada (1985). These formulas describe the displacement field on the surface of an elastic half-space when a dislocation of a specific size and direction is introduced at a given epicentral depth. To transfer the deformation to the free surface, it is assumed that the water layer above behaves as an incompressible medium, and the deformation of the seabed is directly transmitted to the ocean's free surface, following the principles outlined by Kajiura (1970). In order to compute the deformation of the seabed, information regarding the earthquake mechanism is necessary. This includes the fault plane parameters, such as orientation and dimensions, as well as the magnitude of the earthquake and the distribution of slip along the fault plane. The fault plane parameters consist of several key values: the length ( $L$ ) and width ( $W$ ) of the fault plane, the slip (dislocation) along the fault plane, and the angles known as strike, dip, rake, and depth. The length and width represent the dimensions or extensions of the fault plane. The strike angle is measured clockwise relative to the north on a horizontal plane and indicates the direction or trend of the fault. The dip angle measures the inclination or slope of the fault plane from the horizontal surface. The rake angle specifies the direction of movement along the fault plane during a rupture, measured counterclockwise relative to the strike direction. The slip or dislocation along the fault plane is the distance of relative movement along the rake direction and is measured in meters. It represents the amount of displacement or offset that occurs during an earthquake.

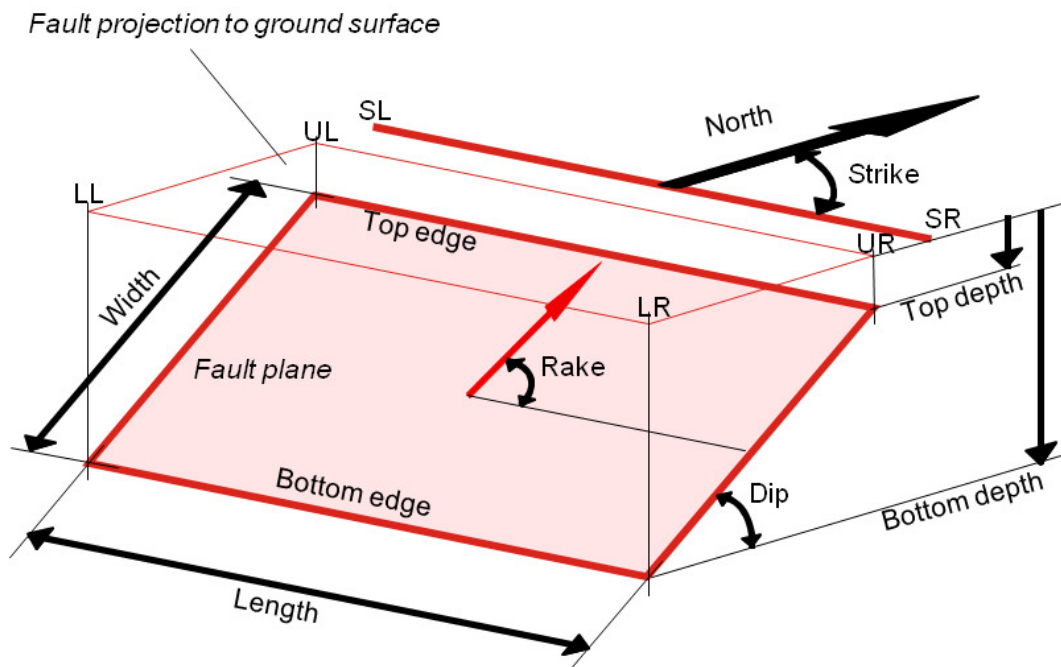


Figure 3.2: Definition of an individual seismogenic source. (Istituto Nazionale di Geofisica e Vulcanologia, 2015)

Figure 3.2 visually represents these fault parameters. Utilizing Okada's model, the initial tsunami condition is calculated based on these variables, and the resulting information is applied to the sea surface to initiate tsunami propagation. The model discussed above has certain limitations that should be acknowledged. Firstly, it simplifies the rupture area to a rectangular shape, which may not accurately represent the actual shape of the fault. Additionally, the model assumes an instantaneous rupture process, which may not be suitable for tsunami earthquakes that exhibit slower rupture mechanisms. Studies conducted by Dutykh and Dias (2007) as well as Dutykh (2008) have demonstrated the inadequacy of this model in such cases. However, in the present study, the application of the model is justified due to specific circumstances. It has been previously employed for medium-sized thrust faults,

where an instantaneous rupture can be reasonably assumed (Omira, 2010). While it is important to recognize the limitations of the model, its utilization in this study is deemed appropriate given the nature of the faults being investigated and the assumptions made regarding the rupture process. The seismic moment ( $M_0$ ), as described by Aki (1972), is a measure of the total energy released during an earthquake. It is determined by the shear modulus ( $\mu$ ), the rupture area ( $A$ ), and the slip ( $D$ ) along the fault plane. The equation representing the seismic moment is as follows:

$$M_0 = \mu \cdot A \cdot D \quad (3.1)$$

In this equation,  $\mu$  represents the shear modulus in pascals (Pa),  $A$  represents the rupture area in square meters ( $m^2$ ), and  $D$  represents the mean slip on  $A$  in meters (m). It is important to note that while the seismic moment depends on all three factors, only two of them directly influence tsunami generation. The slip parameter describes the dislocation or movement along the fault plane, and greater slip values tend to result in larger tsunami wave amplitudes. On the other hand, the rupture area influences the period of the tsunami waves, with larger fault areas producing higher periods. The shear modulus ( $\mu$ ) is a property of the crust in the region and does not have a direct impact on tsunami generation. It primarily affects the seismic moment ( $M_0$ ) and the moment magnitude ( $M_w$ ) associated with the earthquake. The moment magnitude, derived by Kanamori (1977), quantifies the strength of the earthquake. It is closely linked to the scalar seismic moment ( $M_0$ ). One advantage of the moment magnitude scale is that it does not saturate for earthquakes stronger

than magnitude 8, unlike some other magnitude scales. The moment magnitude ( $M_w$ ) is calculated using the formula:

$$M_w = 2 \log_{10}(M_0) - 10.73 \quad (3.2)$$

Tables 4.1, 4.6, 4.10, 3.14 provide a summary of all the fault parameters used to compute the initial conditions for the different tsunami events (1941, 1975, 1980, 1969, respectively). The initial conditions for all the considered tsunami scenarios were computed using the Mirone suite (Luis, 2007), which utilizes Okada's (1985) model.

### 3.4 Tsunami Propagation and SWEs

The motion of viscous fluids can be described by the Navier-Stokes Equations, which are derived from Newton's second law of conservation of momentum in three dimensions. When combined with the conservation of mass, a system of four coupled nonlinear partial differential equations is formed, involving three velocity components and pressure. Unfortunately, there is no complete analytical solution for this coupled system of equations. Hence, approximations are necessary to obtain the best possible solutions, depending on the scale of the geophysical process being studied. In this thesis, the shallow water approximation, and relative equations (SWEs), are employed, which neglect viscous forces as well as the vertical components of velocity and acceleration, and averages horizontal components of velocity over the water column depth. Other models used to simulate tsunamis include the Boussinesq long

wave model and the complete fluid dynamic model. However, the SWEs remain the most commonly used model in computational codes. Over the past two decades, various numerical codes such as TUNAMI-N2 (Imamura, 1995), MOST (Titov and Synolakis, 1995; 1998), COMCOT (Liu et al., 1998), and more recently, UNIBO-TSUFDF (Tonini et al., 2011; Tinti et al., 2013) have been developed to accurately model tsunami propagation and coastal impact. These codes utilize the model presented by Okada (1985) to initiate the propagation. However, they employ different numerical methods to solve the SWEs. In this study, the recently developed and benchmarked code NSWING (Non-linear Shallow Water Model with Nested Grids) (Miranda et al., 2014) is utilized. NSWING has undergone benchmarking following the definitions presented by Synolakis (2006). It is implemented in the C programming language and incorporates core parallelization techniques to enhance computational performance. In Cartesian frame  $(x,y,z)$ , the three Navier-Stokes equations, denoted as (3.3a), (3.3b), and (3.3c), in combination with the equation of conservation of mass (3.3d), form a system of four coupled non-linear partial differential equations.

$$\rho \left( \frac{du}{dt} + f_* w - f v \right) = -\frac{\partial p}{\partial x} + \frac{\partial \tau_{xx}}{\partial x} + \frac{\partial \tau_{yx}}{\partial y} + \frac{\partial \tau_{zx}}{\partial z} \quad (3.3a)$$

$$\rho \left( \frac{dv}{dt} + f u \right) = -\frac{\partial p}{\partial y} + \frac{\partial \tau_{xy}}{\partial x} + \frac{\partial \tau_{yy}}{\partial y} + \frac{\partial \tau_{zy}}{\partial z} + \rho f_y \quad (3.3b)$$

$$\rho \left( \frac{dw}{dt} - f_* u \right) = -\frac{\partial p}{\partial z} + \frac{\partial \tau_{xz}}{\partial x} + \frac{\partial \tau_{yz}}{\partial y} + \frac{\partial \tau_{zz}}{\partial z} + \rho f_z \quad (3.3c)$$

$$\frac{\partial \rho}{\partial t} + \frac{\partial(\rho u)}{\partial x} + \frac{\partial(\rho v)}{\partial y} + \frac{\partial(\rho w)}{\partial z} = 0 \quad (3.3d)$$

Where  $x$ -,  $y$ -, and  $z$ -axes represent the coordinates in the eastward, northward, and upward directions, respectively. The variables  $u$ ,  $v$ , and  $w$  represent the velocity components in the  $x$ ,  $y$ , and  $z$  directions. The term  $f = 2\Omega \sin \phi$  denotes the Coriolis parameter, where  $\phi$  is the latitude. The reciprocal Coriolis parameter, denoted as  $f^* = 2\Omega \cos \phi$ , is often neglected in most tsunami approximations. Here,  $\Omega$  represents the rotation rate of the Earth. Additionally,  $\rho$  denotes the density,  $p$  represents the pressure,  $g$  represents the gravitational acceleration, and the terms  $\tau$  represent normal and shear stresses due to friction. As already mentioned, in the SWEs viscous stresses and vertical flow gradients are neglected, which is considered a valid approximation for long waves, satisfying the condition  $h \leq \lambda$  (Synolakis, 2006). The water body is assumed to be incompressible. The SWEs are derived by integrating the equations over the depth of the water column, from the ocean bottom to the free surface. It is assumed that the pressure distribution is hydrostatic everywhere. This allows for the introduction of the variable  $\eta$ , representing the free surface elevation, through the hydrostatic approximation for pressure,  $p = \rho g(d + \eta)$ , where  $d$  is the

water depth. This assumption is valid and provides results with sufficient accuracy, as tsunamis are considered to be long waves propagating in shallow water. The shallow water model calculates the evolution of the water surface and the depth-averaged water particle velocity. The SWEs may be used in their linear or non-linear form. These linearized equations are considered valid for open ocean propagation when the wave amplitude is significantly smaller than the ocean depth. The linear version of the SWEs, without considering the Coriolis effect, is represented by equations (3.4a-c). The linear version of the Shallow Water Equations (SWEs) without considering the Coriolis effect can be represented as follows:

$$\frac{\partial \eta}{\partial t} + \frac{\partial P}{\partial x} + \frac{\partial Q}{\partial y} = 0 \quad (3.4)$$

$$\frac{\partial P}{\partial t} + g \frac{\partial \eta}{\partial x} = 0 \quad (3.5)$$

$$\frac{\partial Q}{\partial t} + g \frac{\partial \eta}{\partial y} = 0 \quad (3.6)$$

In the given context, the following variables are defined:

$\eta$  : the free-surface displacement

$D = d + \eta$  : the total water depth

$d$  : the still-water depth

$P$  : the horizontal component of the volume flux along the  $x$ -coordinate

$Q$  : the horizontal component of the volume flux along the  $y$ -coordinate

$g$  : the gravitational acceleration

The non-linear shallow water equations (SWEs) account for non-linear convective inertia forces and bottom friction, which become more significant as a tsunami propagates into shallower water. The NSWING model is capable of solving both linear and non-linear SWEs. In this study, non-linear solutions have been computed for all time instants using the DTHA approach. The non-linear SWEs are represented by Equations (3.7, 3.8, 3.9).

$$\frac{\partial \eta}{\partial t} + \frac{\partial P}{\partial x} + \frac{\partial Q}{\partial y} = 0 \quad (3.7)$$

$$\frac{\partial P}{\partial t} + \frac{\partial}{\partial x} \left( \frac{P^2}{D} \right) + gD \frac{\partial \eta}{\partial x} + \tau_x = 0 \quad (3.8)$$

$$\frac{\partial Q}{\partial t} + \frac{\partial}{\partial x} \left( \frac{PQ}{D} \right) + \frac{\partial}{\partial y} \left( \frac{Q^2}{D} \right) + gD \frac{\partial \eta}{\partial y} + \tau_y = 0 \quad (3.9)$$

In spherical coordinates including Coriolis parameter the coupled system of equations yields

$$\frac{\partial \eta}{\partial t} + \frac{1}{r \cos(\phi)} \left( \frac{\partial P}{\partial \psi} + \frac{\partial(\cos(\phi Q))}{\partial \phi} \right) = 0 \quad (3.10)$$

$$\frac{\partial P}{\partial t} + \frac{1}{r \cos(\phi)} \frac{\partial}{\partial \psi} \left( \frac{P^2}{D} \right) + \frac{1}{r} \frac{\partial}{\partial \phi} \left( \frac{PQ}{D} \right) + \frac{gD}{r \cos(\phi)} \frac{\partial \eta}{\partial \psi} - fQ + \tau_x = 0 \quad (3.11)$$

$$\frac{\partial Q}{\partial t} + \frac{1}{r \cos(\phi)} \frac{\partial}{\partial \psi} \left( \frac{PQ}{D} \right) + \frac{1}{r} \frac{\partial}{\partial \phi} \left( \frac{Q^2}{D} \right) + \frac{gD}{r} \frac{\partial \eta}{\partial \psi} + fP + \tau_y = 0 \quad (3.12)$$

where  $\eta$  is the free-surface displacement,  $t$  is time,  $r$  is the radius of the Earth,  $\psi$  is the longitude, and  $\phi$  is the latitude. The total water depth  $D$  is given by  $D = d + \eta$ , where  $d$  is the still-water depth. The bottom friction terms are evaluated by the

Manning formula.

$$\tau_x = \frac{gn^2}{D^{7/3}} P \sqrt{P^2 + Q^2} \quad (3.13)$$

$$\tau_y = \frac{gn^2}{D^{7/3}} Q \sqrt{P^2 + Q^2} \quad (3.14)$$

The Manning's formula is an empirical model that approximates different roughness conditions by applying various roughness coefficients based on the bottom conditions (Linsley and Franzini, 1979). In the case of extreme events like tsunamis, a Manning's roughness coefficient of zero is typically used (Omira, 2010). To numerically solve the presented shallow water equations (SWEs), a process of discretization is employed. This involves replacing the derivatives in the SWEs with finite difference approximations. The problem is modeled on a grid with finite cells, following a grid model scheme. The SWEs are discretized, resulting in an algebraic system of equations that can be solved iteratively. At each time step, the discretized algebraic equations are solved for each cell  $(i, j)$  based on the conditions from the previous time step. The initial condition sets the system in motion at time step  $t = 0$ . For linear terms, NSWING utilizes an explicit staggered finite leapfrog numerical scheme (Liu et al., 1998), while for non-linear terms, an upwind scheme is employed. The choice of the time step must satisfy the Courant-Friedrichs-Lewy (CFL) condition to ensure numerical stability. The linear CFL condition is expressed by equation (3.15),

and NSWING adopts a maximum CFL value of 0.5.

$$\text{CFL} = u * \frac{\Delta t}{\Delta x} \leq C_{\max} \quad (3.15)$$



## Chapter 4

# Application of the Decision Matrix to the 20th century tsunamis along the Gloria Fault

As already introduced in sections 1.3 and 1.4, the Gloria fault is a major geological fault that runs along the coast of the Iberian Peninsula and the western Mediterranean Sea. Throughout the 20th century, there were several notable tsunamis that were associated with this fault. In this section some of the biggest tsunamis will be analyzed and modeled, some of them generated by a strike-slip mechanism, such as the 25 November 1941, 26 May 1975 and 1 January 1980 tsunamis, and one by a dip-slip mechanism, the 28 February 1969 tsunami, which occurred in the south-west Iberian margin, outside the Gloria Fault. To further investigate the applicability of the Decision Matrix (DM) to the specific case of strike-slip events, a comparative

analysis has been conducted. For each strike-slip event, a corresponding dip-slip scenario has been modeled, maintaining identical epicenter location and magnitude, while only altering the focal mechanism by adjusting the rake angle. By examining the obtained results for different wave heights in these two scenarios, valuable insights can be gained regarding the suitability of the DM for each case. This analysis aims to determine if the DM exhibits a stronger applicability or correlation with one of the scenarios, providing a better understanding of its effectiveness in assessing the impact of strike-slip events.

## **4.1 25 November 1941 event**

### **4.1.1 1941 strike-slip event**

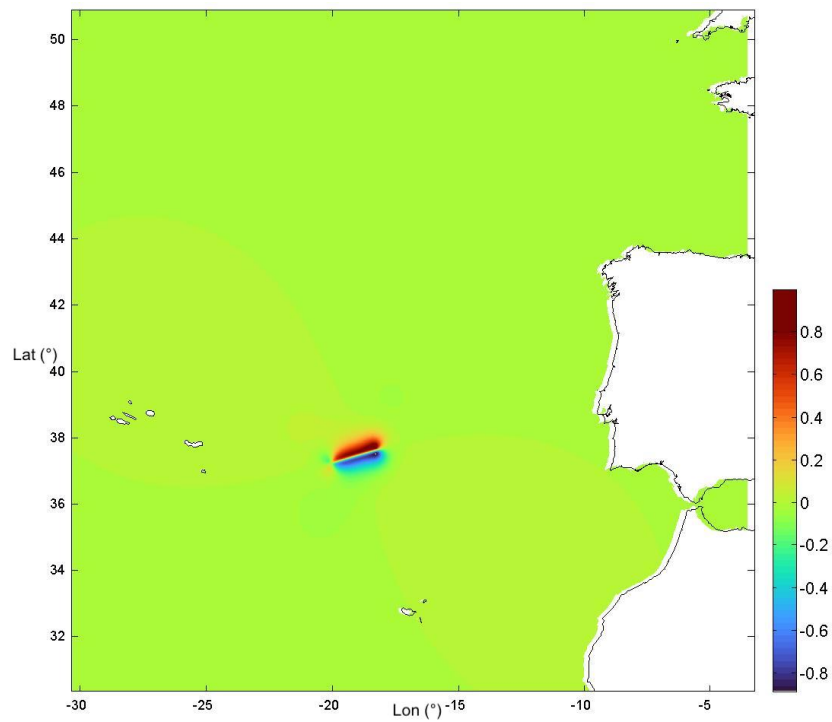
The earthquake that occurred on November 25, 1941 at 18:03:54 UTC, impacted Madeira, Azores, and western Portugal, where the strongest shaking resulted in an intensity of VI (MSK) (Baptista et al. 2016). It also affected neighboring countries, Spain and Morocco. Furthermore, its effects were observed as far as Newlyn in the United Kingdom, approximately 1800 km away from the epicenter. This observation indicates a basin wide behavior of the tsunami. Several studies, including those by Debrach (1946), Di Filippo (1949), and Moreira (1968), have analyzed macroseismic data related to this earthquake. Antunes (1944) initially determined the epicenter location using data solely from the Portuguese seismic network, which was found to be at coordinates  $-18.9^\circ$  E,  $38.7^\circ$  N. Subsequently, Gutenberg and Richter (1949) re-located the epicenter to  $-18.5^\circ$  E,  $37.50^\circ$  N and calculated the earthquake magnitude

as  $M_s = 8.2$ . Lynnes and Ruff (1985) later refined the epicenter location to  $-19.1^\circ$  E,  $37.6^\circ$  N, employing a master-event technique relative to a better characterized event (May 26, 1975). Udias et al. (1976) determined the earthquake magnitude to be 8.3. In this study, magnitude and the epicentre location selected to model the tsunami are 8.3 and  $-19.038^\circ$  E,  $37.4050^\circ$  N, according to Baptista et al (2019). The same paper discusses the focal mechanism which have been used in this study. In particular, the parameters of the source are presented in table 4.1:

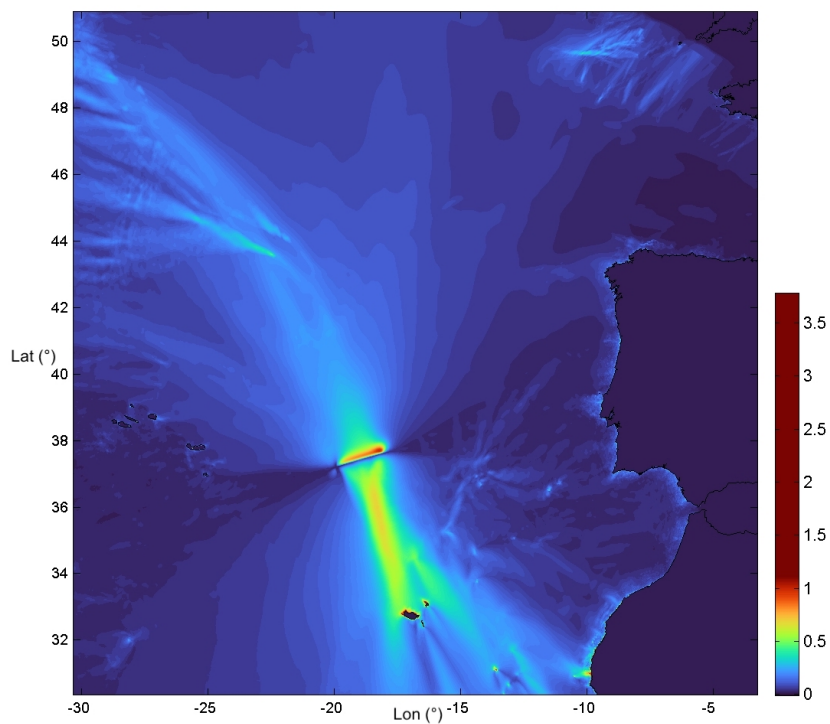
Scenario name	L (km)	W (km)	Epicenter coordinates		D (km)	slip (m)	Strike ( $^\circ$ )	Dip ( $^\circ$ )	Rake ( $^\circ$ )	$\mu$ (GPa)	$M_w$
			Lon	Lat							
1941	170	45	-19.04	37.41	12	8	254	88	161	45	8.3

Table 4.1: Source parameters for the 1941 event (Baptista et al., 2016), L: the fault length in kilometers; W: the fault width in kilometers; D: the depth from the sea bottom to the top of the fault in kilometers;  $\mu$ : the shear modulus and  $M_w$ : the moment magnitude.

Baptista et al. (2016) present a comprehensive analysis of the data, which have been checked with the non linear shallow water code implemented in Mirone software, using the same epicentre and magnitude as the ones used in the study. The set of tsunami data which have been compared include records from eight stations available in UK, Azores and Madeira islands, Morocco (Casablanca and Essaouira) and three stations in mainland Portugal (Ponta Delgada, Leixões), Tab. 4.2:



(a)



(b)

Figure 4.1: Tsunami numerical simulation for the 1941 strike-slip event. (a) The initial sea-surface perturbation (m) that follows the sea-bottom deformation. (b) The maximum tsunami wave heights (m) distribution.

Magnitude	Lon. and Lat. (°E , °N)	Max. amplitude (Dip) (m)
Ponta Delgada	-25.65, 37.73	0.20
Madeira	-16.91, 32.63	0.63
Leixões	-8.71, 41.17	0.20
Cascais	-9.41, 38.69	0.11
Casablanca	-7.59, 33.62	0.09
Essaouira	-9.78, 31.51	0.12
Lagos	-8.66, 37.10	0.12

Table 4.2: *POIs (points of interest) of the 1941 tsunami, recorded maximum amplitude associated (M.A. Baptista, 2016).*

The figures presented below illustrate the computed wave profiles for the selected point of interest. In particular in all the simulations these have been selected as the grid nodes located closer to the real tide gauges. Notably, Table 4.3 provides details regarding the maximum detected wave height obtained from the model’s analysis.

Magnitude	Lon. and Lat. (°E , °N)	Max. amplitude (Dip) (m)
Ponta Delgada	-25.65, 37.73	0.09
Madeira	-16.91, 32.63	0.71
Leixões	-8.71, 41.17	0.20
Cascais	-9.41, 38.69	0.14
Casablanca	-7.59, 33.62	0.12
Essaouira	-9.78, 31.51	0.34
Lagos	-8.66, 37.10	0.16

Table 4.3: *POIs (points of interest) of the 1941 tsunami used in the simulation, maximum amplitude associated.*

#### 4.1.2 1941 dip-slip scenario

To evaluate the coherence between the Decision matrix and dip-slip events, a simulated dip-slip scenario was constructed to compare its outcomes with the actual case.

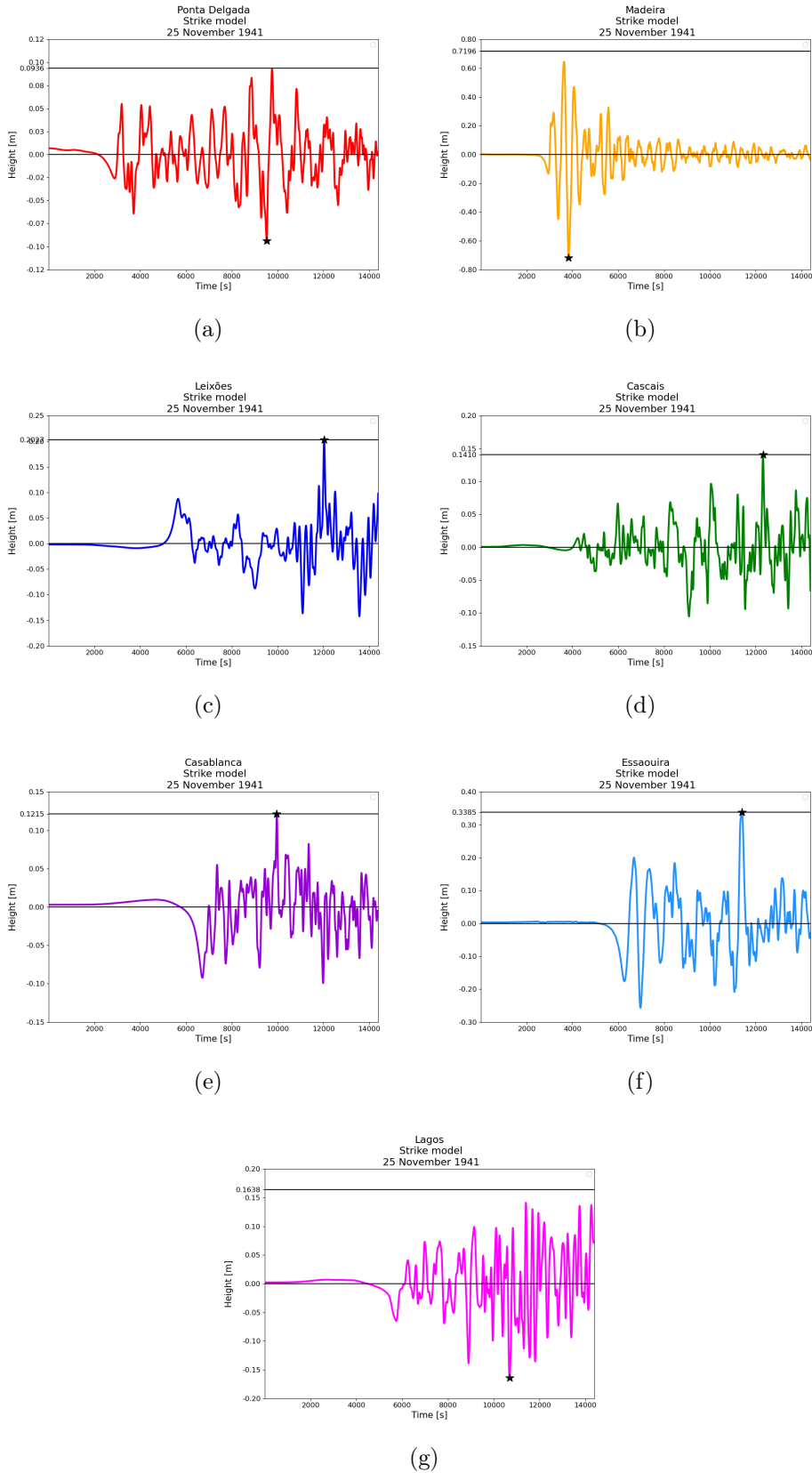


Figure 4.2: Modeled waveforms for the 1941 strike-slip event. (a-g) indicates in order the stations in table 4.3. The star denotes the highest amplitude of the modeled waveform, and its absolute value is represented by the solid black line.

The modeling process involved maintaining fixed source parameters while varying only the rake value, as outlined in Table 4.4.

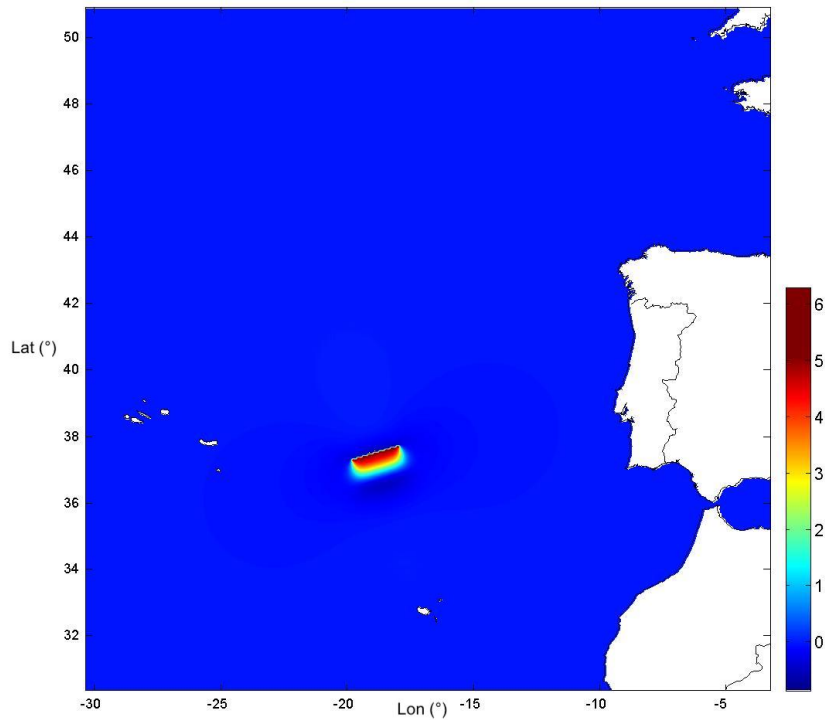
Scenario name	L (km)	W (km)	Epicenter coordinates		D (km)	slip (m)	Strike (°)	Dip (°)	Rake (°)	$\mu$ (GPa)	$M_w$
			Lon	Lat							
1941	170	45	-19.04	37.41	12	8	254	88	90	45	8.3

Table 4.4: Source parameters for the 1941 dip-slip scenario, L: the fault length in kilometers; W: the fault width in kilometers; D: the depth from the sea bottom to the top of the fault in kilometers;  $\mu$ : the shear modulus and  $M_w$ : the moment magnitude.

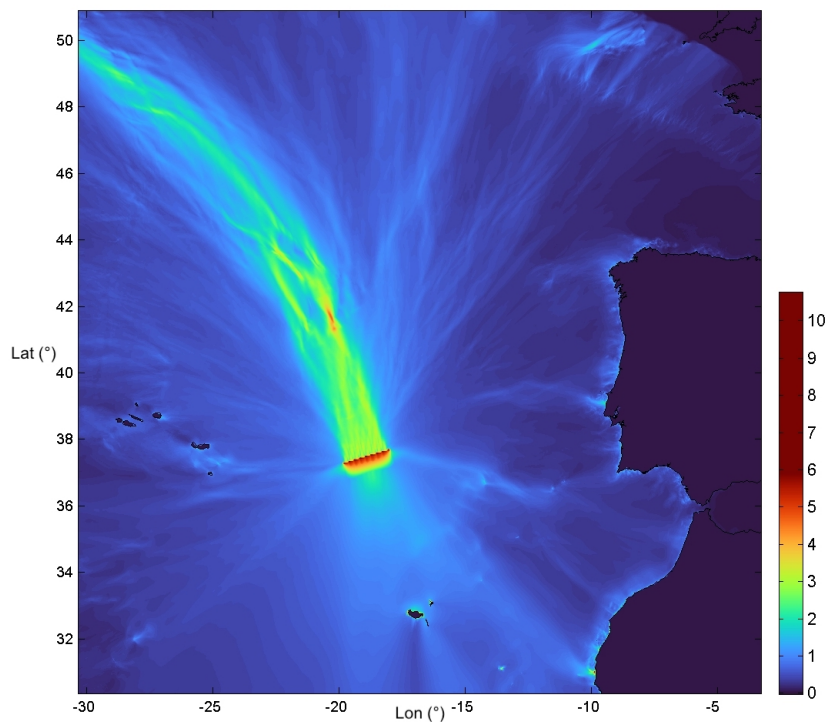
Magnitude	Lon. and Lat. (°E , °N)	Max. amplitude (Dip) (m)
Ponta Delgada	-25.65, 37.73	0.50
Madeira	-16.91, 32.63	2.01
Leixões	-8.71, 41.17	0.36
Cascais	-9.41, 38.69	0.34
Casablanca	-7.59, 33.62	0.39
Essaouira	-9.78, 31.51	0.65
Lagos	-8.66, 37.10	0.45

Table 4.5: *POIs (points of interest) of the 1941 tsunami used in the dip-slip scenario, maximum amplitude associated.*

After simulating two scenarios, a real strike-slip and a dip-slip earthquake, the maximum wave heights were obtained and compared to the decision matrix (Table 2.5) to determine the appropriate alert level (watch, advisory, information according to ICG/NEAMTWS). The analysis focused on the magnitude of the 1941 earthquake (8.3), and the resulting alert levels from the DM for the stations are illustrated in Figure 4.5. Alert levels which derive from the simulations are shown in figure 4.6.

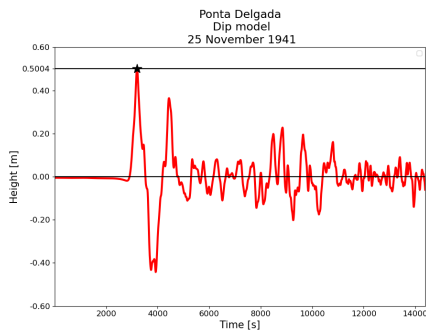


(a)

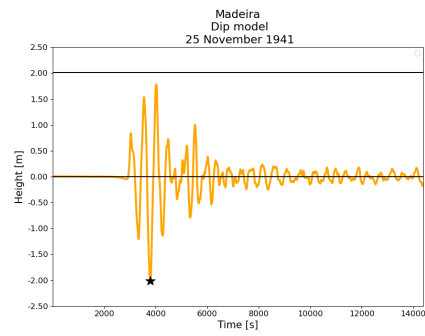


(b)

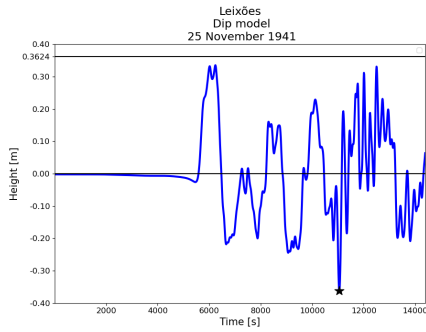
Figure 4.3: Tsunami numerical simulation for the 1941 dip-slip scenario. (a) The initial sea-surface perturbation (m) that follows the sea-bottom deformation. (b) The maximum tsunami wave heights (m) distribution.



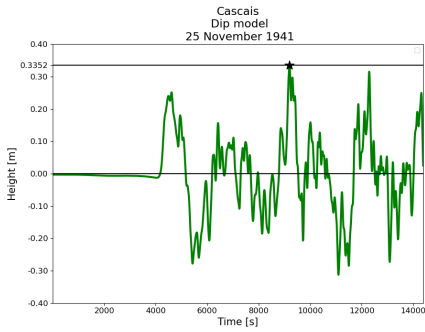
(a)



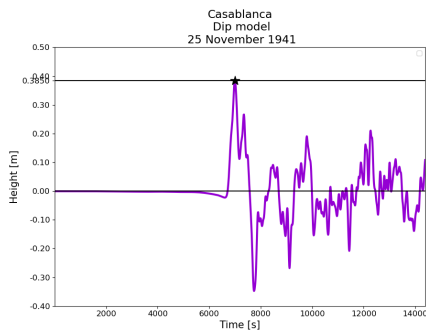
(b)



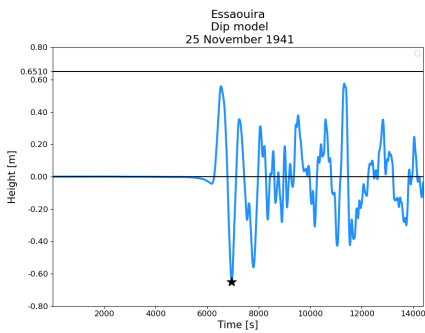
(c)



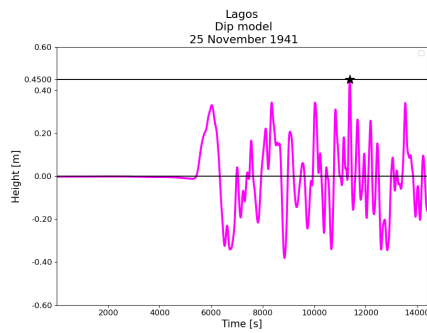
(d)



(e)



(f)



(g)

Figure 4.4: Modeled waveforms for the 1941 dip-slip event. (a-g) indicates in order the stations in table 4.2. The star denotes the highest amplitude of the modeled waveform, and its absolute value is represented by the solid black line.

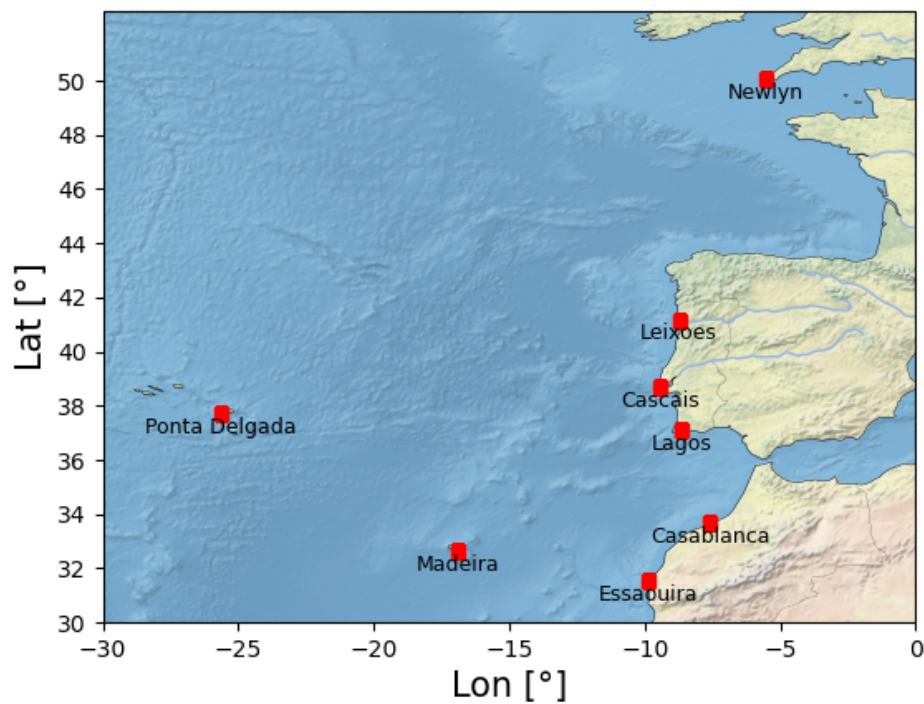


Figure 4.5: Expected alert levels for stations for the 1941 earthquake (magnitude 8.3). The alert levels (ICG/NEAMTWS) are determined by comparing the wave height values to the decision matrix (Table 2.5). In particular the choice of colors indicates: green=information, orange=advisory, red=watch, following the indication of table 2.3.

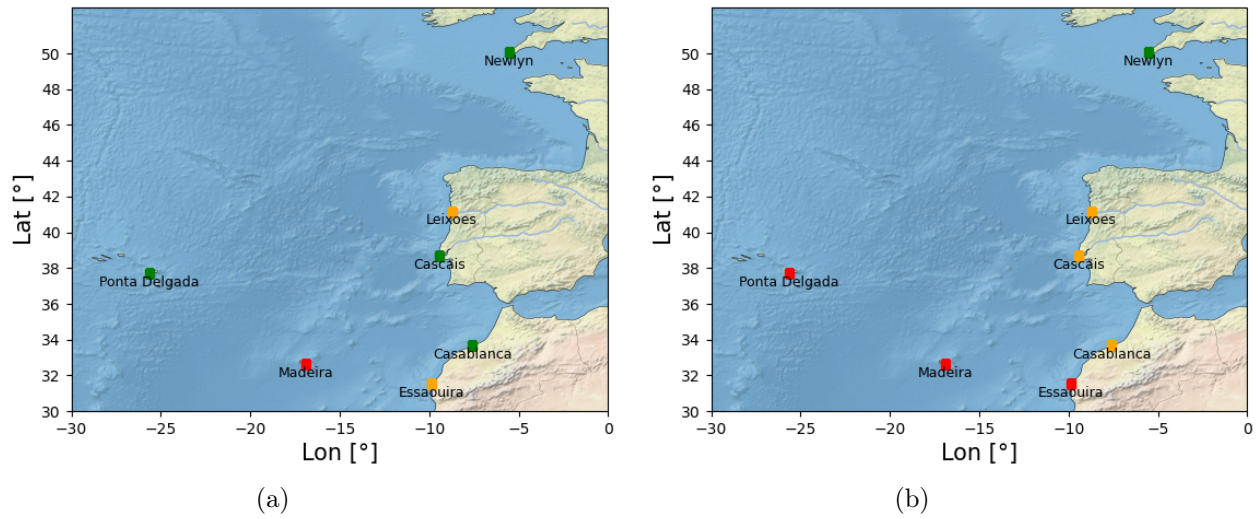


Figure 4.6: Comparison of expected alert levels for stations based on maximum wave heights resulting from simulations of the 1941 earthquake (magnitude 8.3), (a) strike-slip scenario, (b) dip-slip scenario. The alert levels (ICG/NEAMTWS) are determined by comparing the maximum wave height values to the decision matrix (Table 2.5). In particular the choice of colors indicates: green=information, orange=advisory, red=watch, following the indication of table 2.3.

## 4.2 26 May 1975 event

### 4.2.1 1975 strike-slip event

The earthquake on 26 May 1975, with a magnitude of  $M_s = 7.9$ , occurred in the North East Atlantic, approximately 200 km south of the Gloria Fault, at a latitude of  $35.9^\circ\text{N}$  and a longitude of  $17.5^\circ\text{W}$  (Kaabouben 2008). Studies on the focal mechanism by Lynnes and Ruff (1985) "*first-motion*" solution and Bufo et al. (1988) concluded for a dextral strike-slip event with no significant dip-slip component, compatible with the relative motion between Eurasia and Nubia plates but 200 km south of the presumed plate boundary. The tsunami was recorded in Portugal and Spain. In table 4.6 the parameters of the source, that will be also used in the simulation, are presented:

Scenario name	L (km)	W (km)	Epicenter coordinates		D (km)	slip (m)	Strike ( $^\circ$ )	Dip ( $^\circ$ )	Rake ( $^\circ$ )	$\mu$ (GPa)	$M_w$
			Lon	Lat							
1975	110	28	-17.48	35.89	26.4	11	288.0	72.0	184.0	40	7.9

Table 4.6: Source parameters (from Baptista et al., 1992) for the 1975 event, L: the fault length in kilometers; W: the fault width in kilometers; D: the depth from the sea bottom to the top of the fault in kilometers;  $\mu$ : the shear modulus and  $M_w$ : the moment magnitude.

Stations that recorded tsunami records are listed in tab. 4.7, with the associate wave maximum:

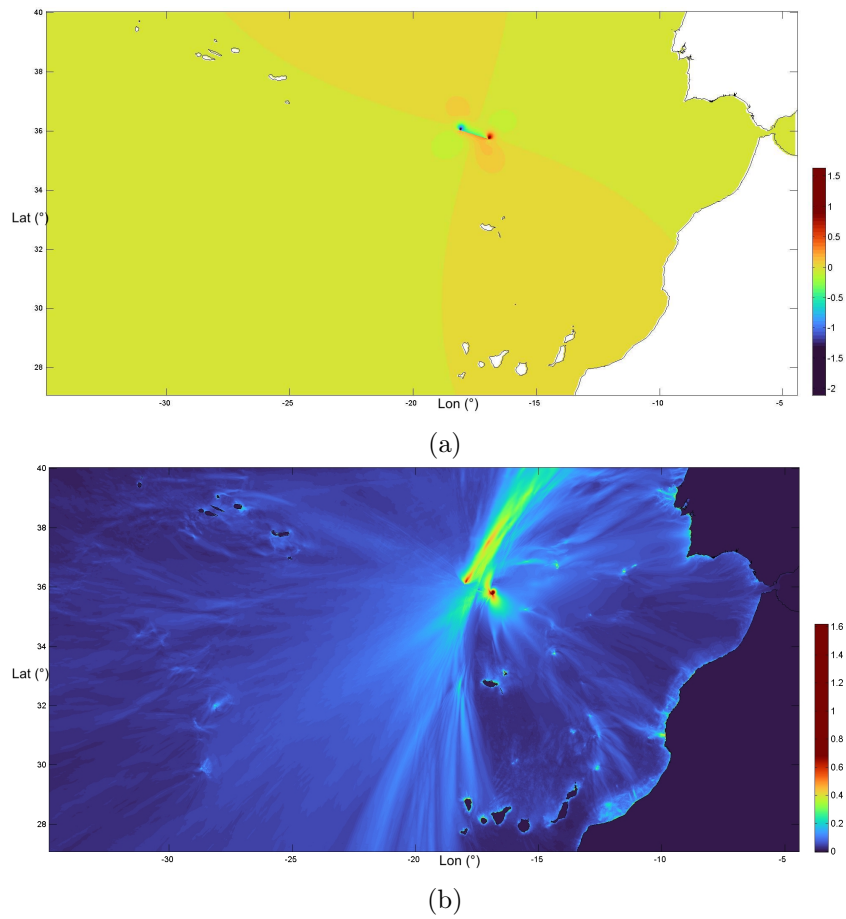


Figure 4.7: Tsunami numerical simulation for the 1975 strike-slip event. (a) The initial sea-surface perturbation (m) that follows the sea-bottom deformation. (b) The maximum tsunami wave heights (m) distribution.

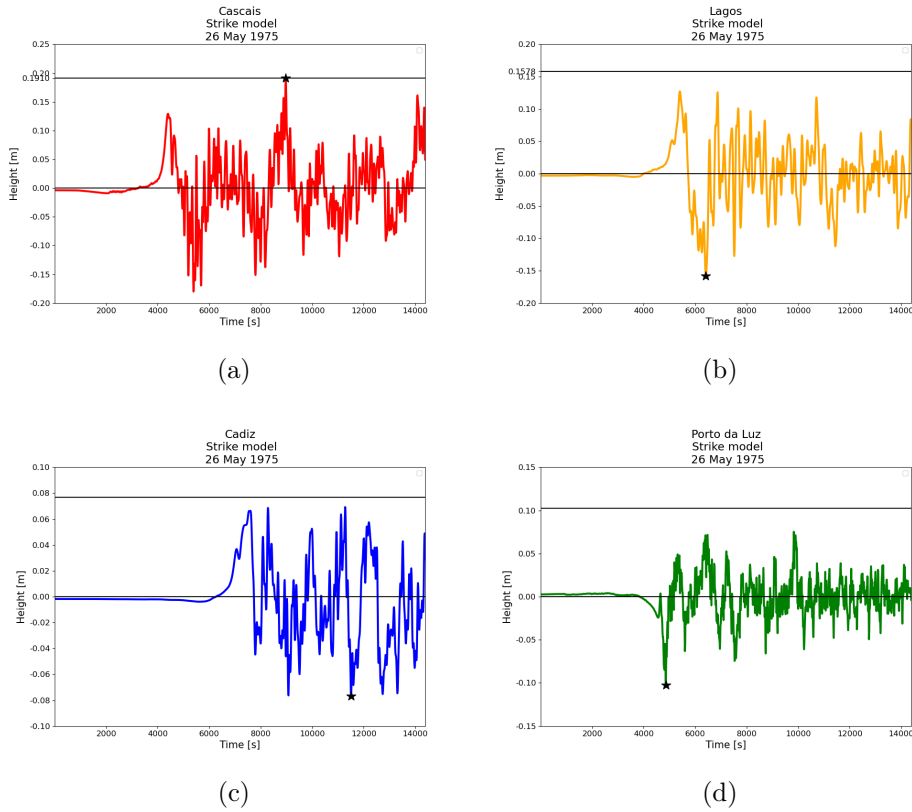


Figure 4.8: Modeled waveforms for the 1975 strike-slip event. (a-d) indicates in order the stations in table 4.7. The star denotes the highest amplitude of the modeled waveform, and its absolute value is represented by the solid black line.

Magnitude	Lon. and Lat. (°E , °N)	Max. amplitude (Dip) (m)
Cascais	-9.41, 38.69	0.07
Lagos	-8.66, 37.10	0.20
Cadiz	-6.29, 36.53	0.11
Porto da Luz	-15.38, 28.12	0.10

Table 4.7: POIs (points of interest) of the 1975 tsunami, recorded maximum amplitude associated (Kaabouben 2008).

Magnitude	Lon. and Lat. (°E , °N)	Max. amplitude (Dip) (m)
Cascais	-9.41, 38.69	0.19
Lagos	-8.66, 37.10	0.16
Cadiz	-6.29, 36.53	0.08
Porto da Luz	-15.38, 28.12	0.10

Table 4.8: *POIs (points of interest) of the 1975 tsunami used in the strike-slip simulation, maximum amplitude associated.*

#### 4.2.2 1975 dip-slip scenario

Magnitude	Lon. and Lat. (°E , °N)	Max. amplitude (Dip) (m)
Cascais	-9.41, 38.69	0.74
Lagos	-8.66, 37.10	0.54
Cadiz	-6.29, 36.53	0.35
Porto da Luz	-15.38, 28.12	0.49

Table 4.9: *POIs (points of interest) of the 1975 tsunami used in the dip-slip scenario, maximum amplitude associated.*

After simulating two scenarios, a real strike-slip and a dip-slip earthquake, the maximum wave heights were obtained and compared to the decision matrix (Table 2.5) to determine the appropriate alert level (watch, advisory, information, according to ICG/NEAMTWS). The analysis focused on the magnitude of the 1975 earthquake (7.9), and the resulting alert levels from the DM for the stations are illustrated in Figure 4.11. Alert levels which derive from the simulations are shown in figure 4.12.

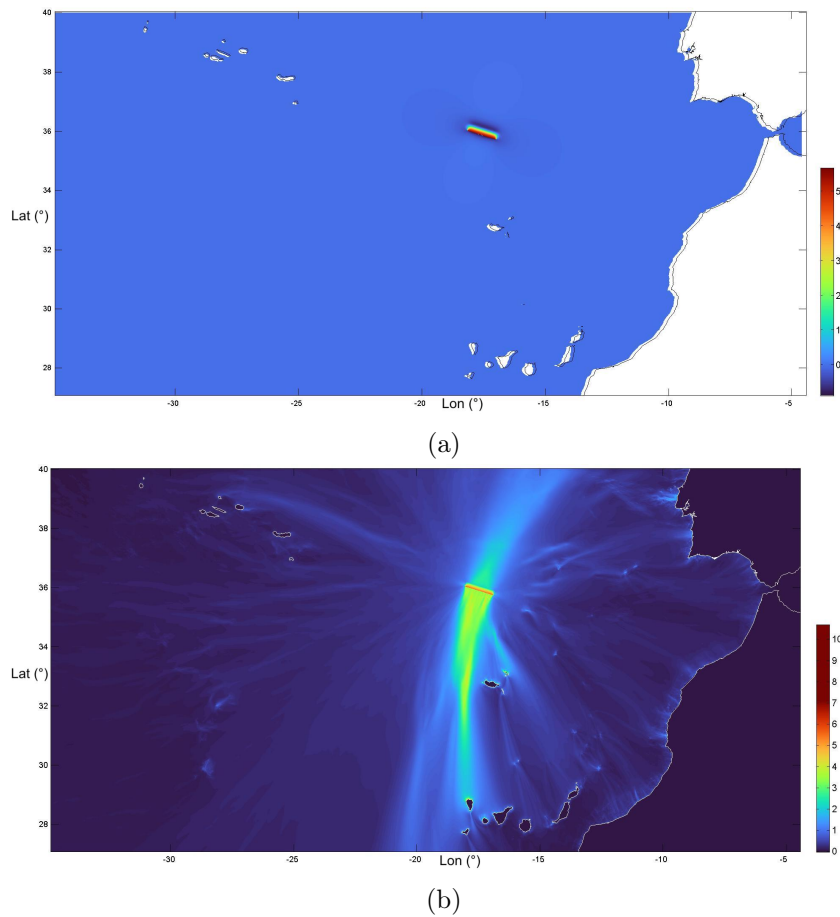


Figure 4.9: Tsunami numerical simulation for the 1975 dip-slip event. (a) The initial sea-surface perturbation (m) that follows the sea-bottom deformation. (b) The maximum tsunami wave heights (m) distribution.

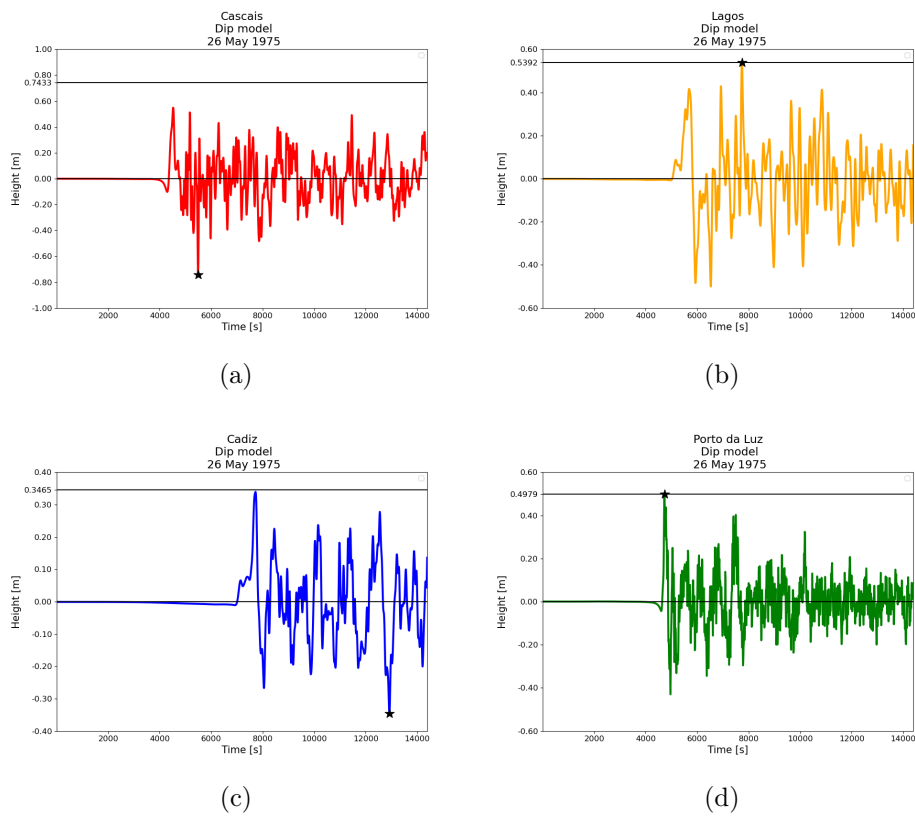


Figure 4.10: Modeled waveforms for the 1975 dip-slip event. (a-d) indicates in order the stations in table 4.7. The star denotes the highest amplitude of the modeled waveform, and its absolute value is represented by the solid black line.

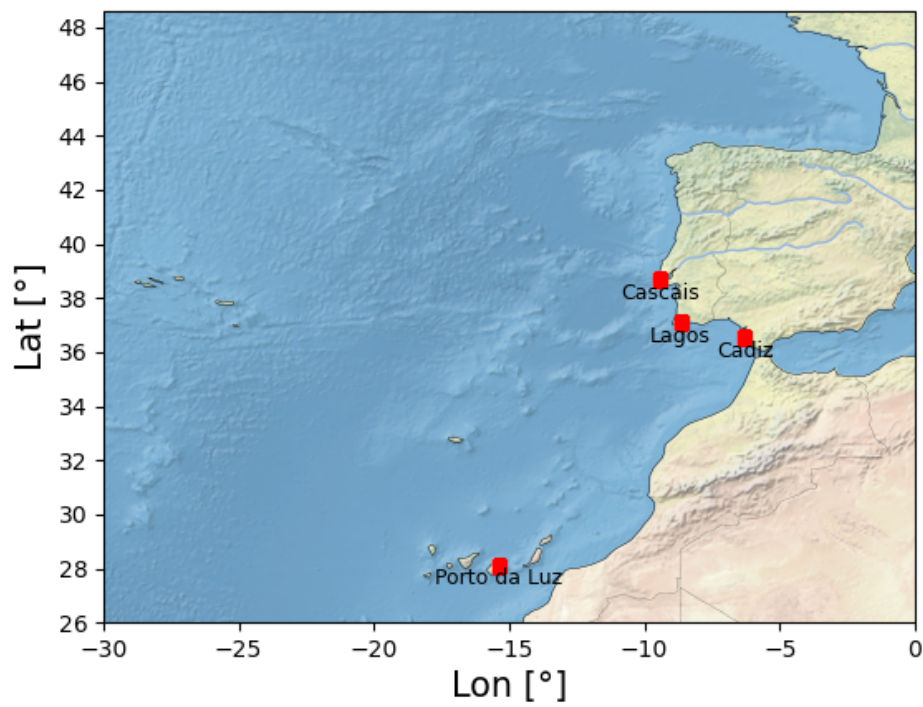


Figure 4.11: Expected alert levels for stations for the 1975 earthquake (magnitude 7.9). The alert levels (ICG/NEAMTWS) are determined by comparing the wave height values to the decision matrix (Table 2.5). In particular the choice of colors indicates: green=information, orange=advisory, red=watch, following the indication of table 2.3.

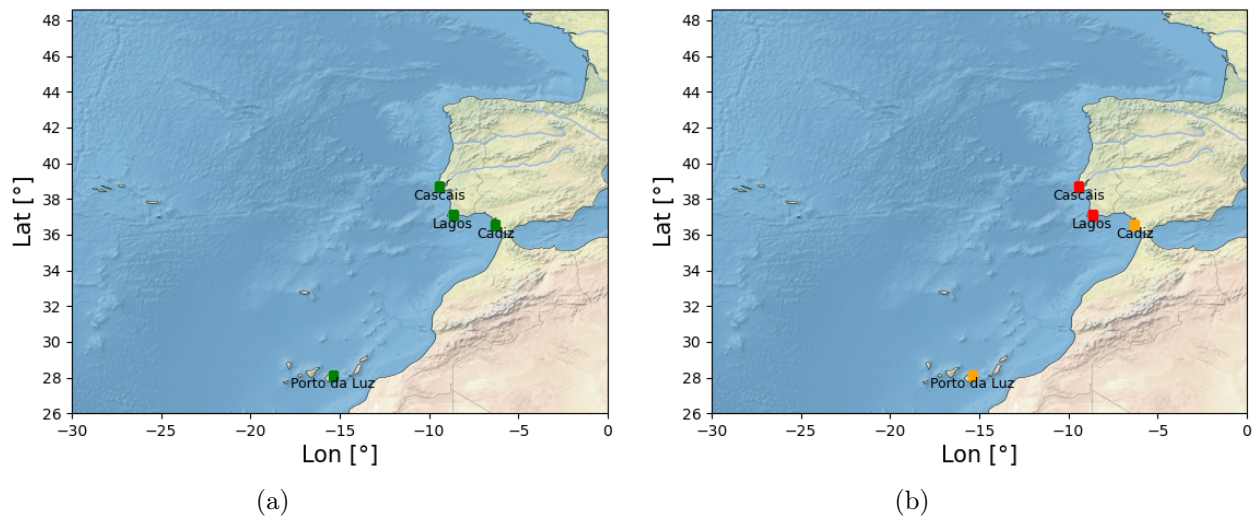


Figure 4.12: Comparison of expected alert levels for stations based on maximum wave heights resulting from simulations of the 1975 earthquake (magnitude 7.9), (a) strike-slip scenario, (b) dip-slip scenario. The alert levels (ICG/NEAMTWS) are determined by comparing the wave height values to the decision matrix (Table 2.5). In particular the choice of colors indicates: green=information, orange=advisory, red=watch, following the indication of table 2.3.

### 4.3 1 January 1980 event

#### 4.3.1 1980 strike-slip event

The epicenter of this earthquake was located between Terceira and San Jorge Islands,  $38.81^\circ\text{N}$ ,  $27.78^\circ\text{W}$ , with a hypocentral depth of 10 km. The origin time was recorded as 16:42, and it had a magnitude of  $M_s = 6.7$  and  $M_w = 6.8$  (Borges 2007). The intensity of the earthquake reached a maximum level of VIII-IX (MM) at "Doze Ribeiras" on Terceira Island ( $38.72^\circ\text{N}$ ,  $27.22^\circ\text{W}$ ). The impact of the earthquake resulted in the loss of 61 lives and injuries to 400 individuals. The old city of Angra do Heroismo on Terceira Island was significantly destroyed, and buildings on Terceira, San Jorge ( $38.64^\circ\text{N}$ ,  $28.4^\circ\text{W}$ ), and Graciosa Islands ( $39.05^\circ\text{N}$ ,  $28.01^\circ\text{W}$ ) suffered severe damage (Machado and Silveira, 1982; Moreira, 1985). Following the main shock, more than 400 aftershocks were recorded, mainly distributed in a narrow band in a N150°E direction (Hirn et al., 1980). The focal mechanism of the main shock has been studied using various techniques, including the first motion of P waves (Buforn et al., 1983 and 1988; Nakanishi and Kanamori, 1984; Moreira, 1985). Grimison and Chen (1988) derived the focal mechanism using WWSSN long-period records and body-wave modeling. In table 4.10 the parameters of the source, that will be also used in the simulation, are presented:

Scenario name	L (km)	W (km)	Epicenter coordinates		D (km)	slip (m)	Strike (°)	Dip (°)	Rake (°)	$\mu$ (GPa)	$M_w$
			Lon	Lat							
1980	54	14	-27.78	38.81	7.0	3.0	149.0	85.0	-2	30	6.8

Table 4.10: Source parameters (from Borges, 2007), L: the fault length in kilometers; W: the fault width in kilometers; D: the depth from the sea bottom to the top of the fault in kilometers;  $\mu$ : the shear modulus and  $M_w$ : the moment magnitude.

Stations that recorded tsunami records are listed in tab. 4.11, with the associate wave maximum:

Magnitude	Lon. and Lat. (°E , °N)	Max. amplitude (m)
Ponta Delgada	-25.65, 37.73	0.07
Horta	-16.91, 32.63	0.25
Angra	-8.71, 41.17	0.05

Table 4.11: *POIs (points of interest) of the 1980 tsunami, maximum amplitude associated.*

Magnitude	Lon. and Lat. (°E , °N)	Max. amplitude (Strike) (m)
Ponta Delgada	-25.65, 37.73	0.05
Horta	-16.91, 32.63	0.23
Angra	-8.71, 41.17	0.05

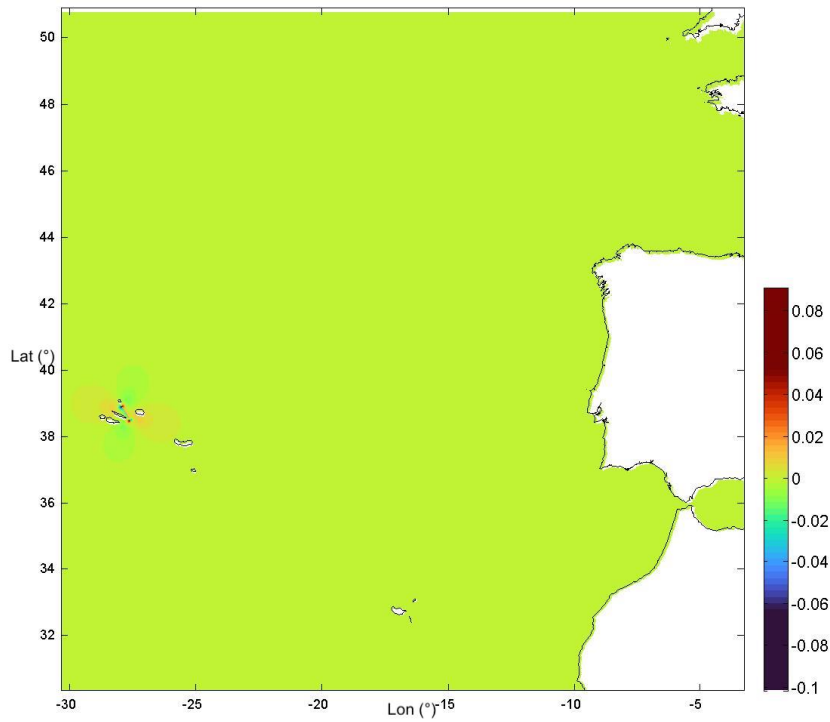
Table 4.12: *POIs (points of interest) of the 1980 tsunami used in the Strike simulation, maximum amplitude associated.*

### 4.3.2 1980 dip-slip scenario

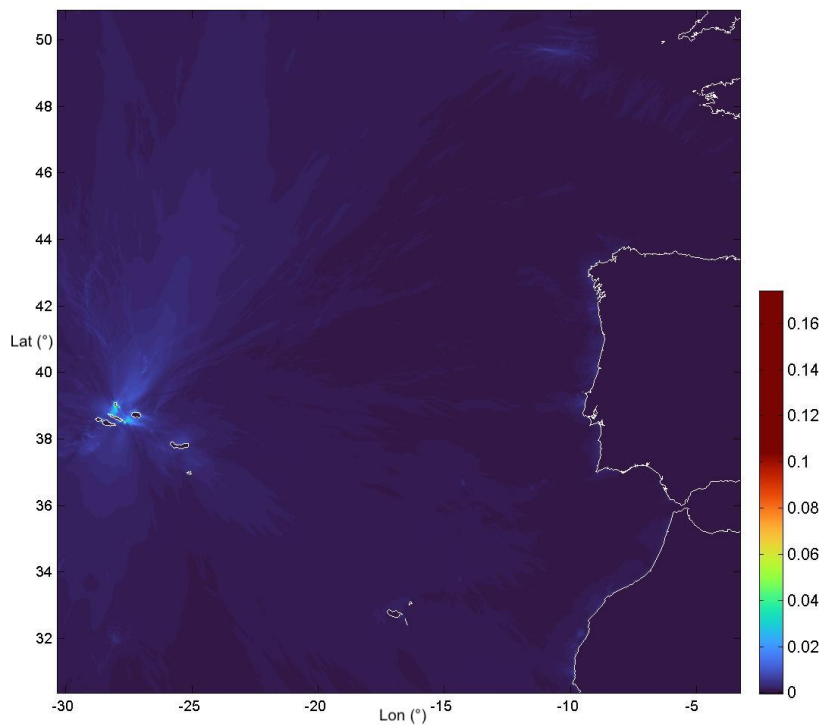
Magnitude	Lon. and Lat. (°E , °N)	Max. amplitude (Dip) (m)
Ponta Delgada	-25.65, 37.73	0.15
Horta	-28.62, 38.53	0.25
Angra	-27.22, 38.65	0.43

Table 4.13: *POIs (points of interest) of the 1980 tsunami used in the Dip simulation, maximum amplitude associated.*

After simulating two scenarios, a real strike-slip and a dip-slip earthquake, the maximum wave heights were obtained and compared to the decision matrix (Table 2.5)



(a)



(b)

Figure 4.13: Tsunami numerical simulation for the 1980 strike-slip event. (a) The initial sea-surface perturbation (m) that follows the sea-bottom deformation. (b) The maximum tsunami wave heights (m) distribution.

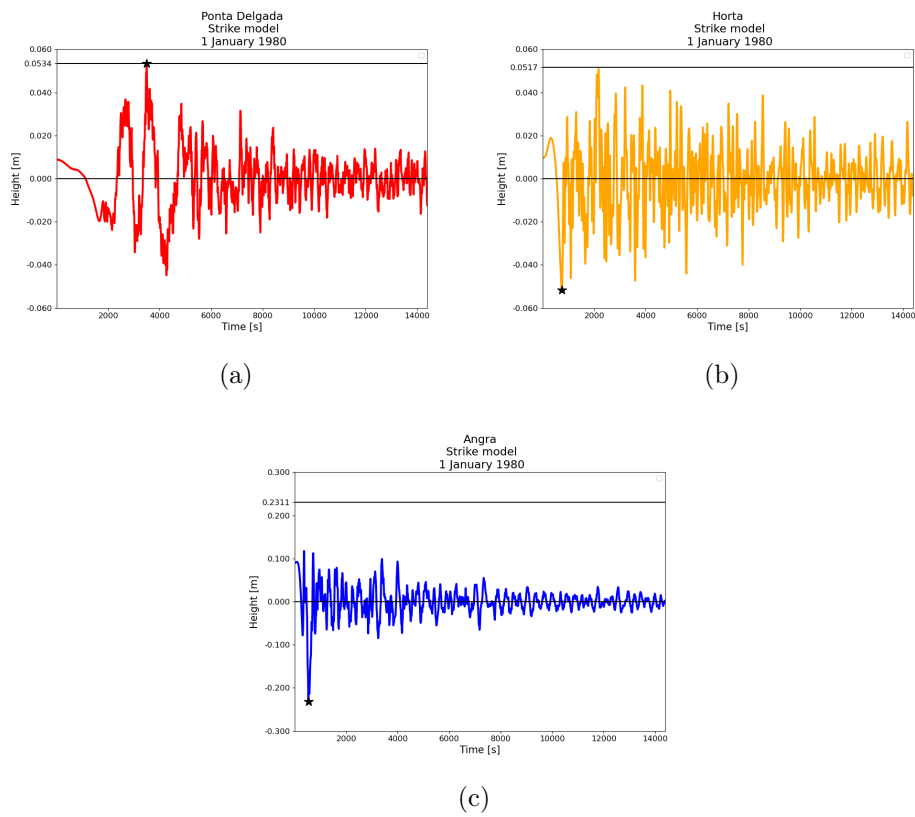
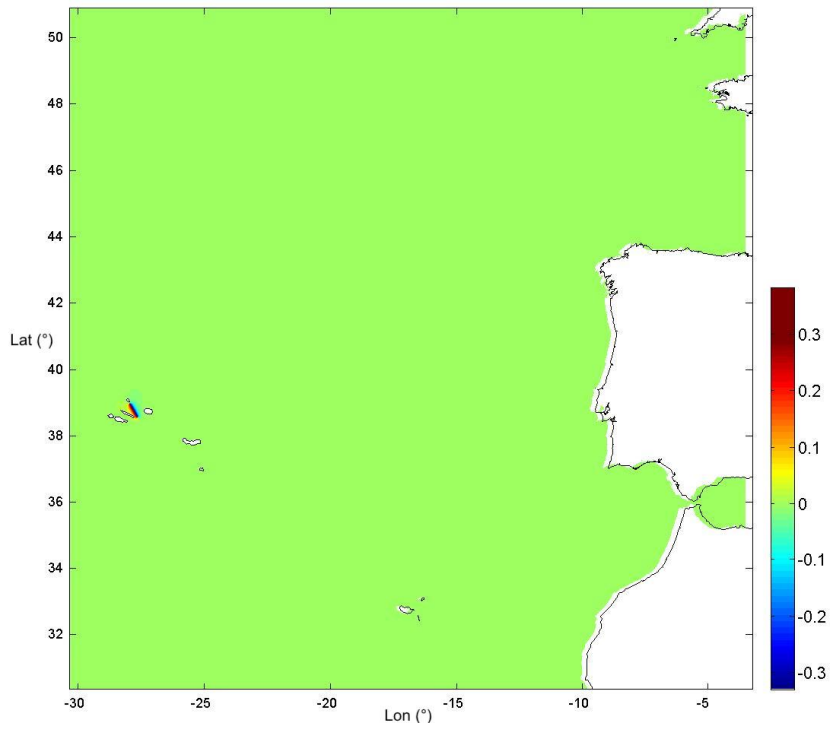
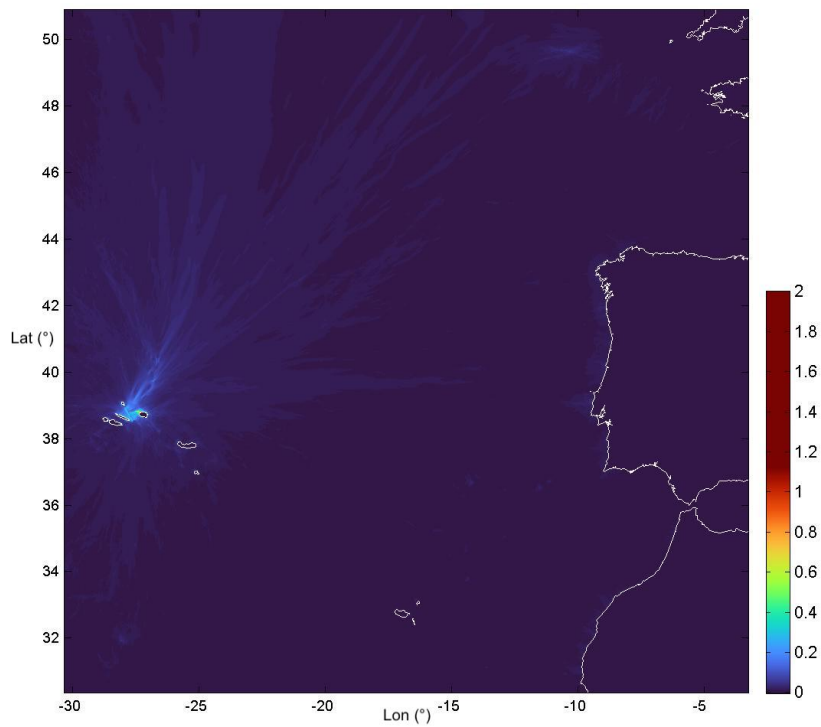


Figure 4.14: Modeled waveforms for the 1980 strike-slip event. (a-c) indicates in order the stations in table 4.11. The star denotes the highest amplitude of the modeled waveform, and its absolute value is represented by the solid black line.



(a)



(b)

Figure 4.15: Tsunami numerical simulation for the 1980 dip-slip event. (a) The initial sea-surface perturbation (m) that follows the sea-bottom deformation. (b) The maximum tsunami wave heights (m) distribution.

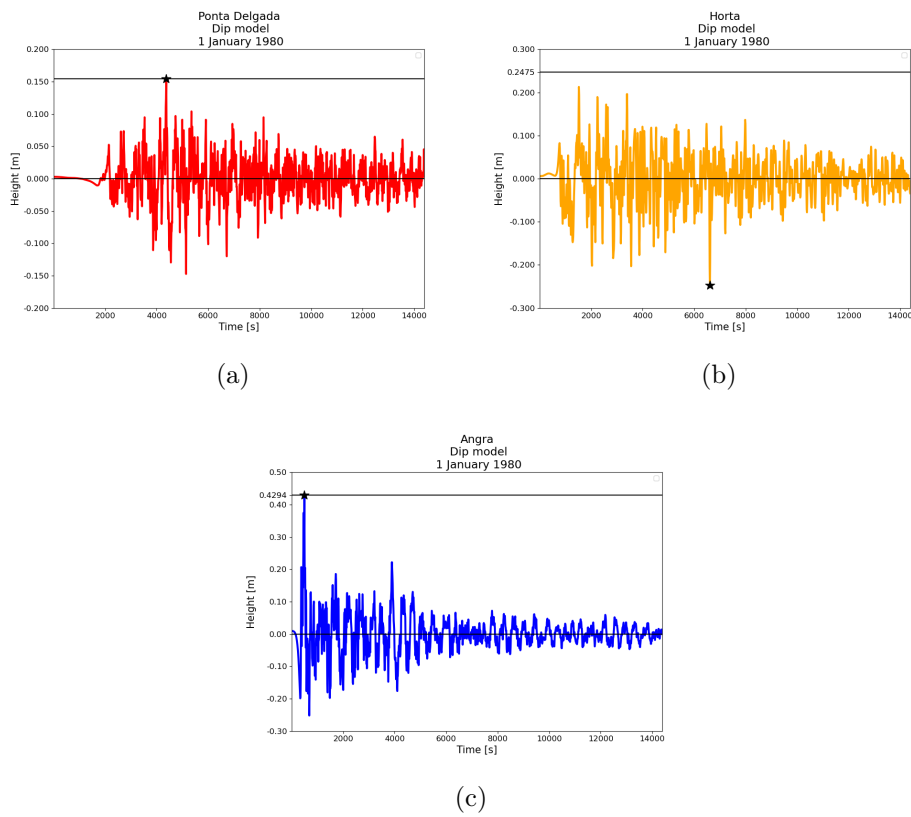


Figure 4.16: Modeled waveforms for the 1980 dip-slip event. (a-c) indicates in order the stations in table 4.11. The star denotes the highest amplitude of the modeled waveform, and its absolute value is represented by the solid black line.

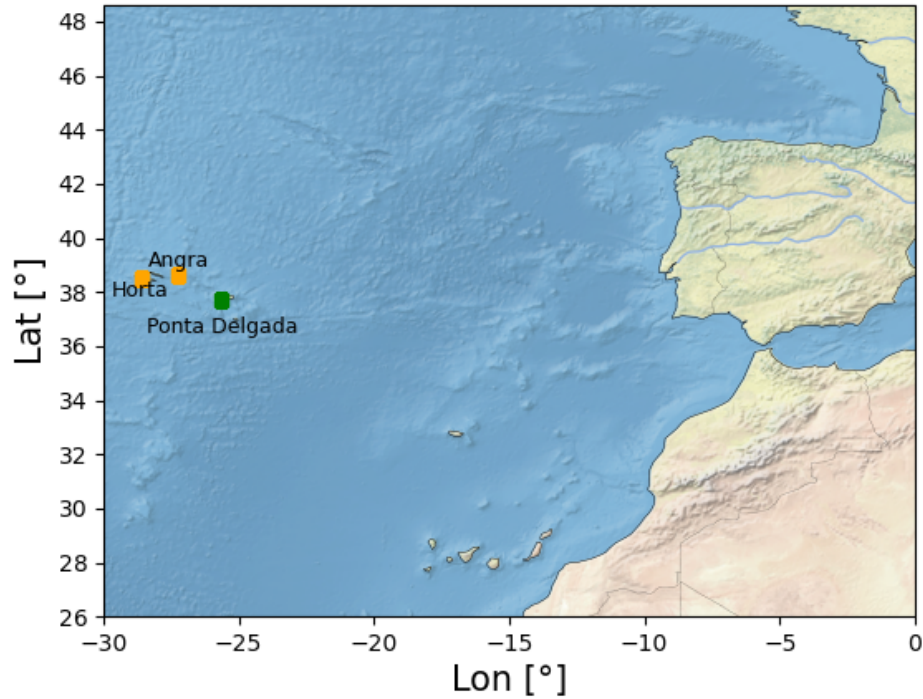


Figure 4.17: Expected alert levels for stations for the 1980 earthquake (magnitude 6.8). The alert levels (ICG/NEAMTWS) are determined by comparing the wave height values to the decision matrix (Table 2.5). In particular the choice of colors indicates: green=information, orange=advisory, red=watch, following the indication of table 2.3.

to determine the appropriate alert level (watch, advisory, information, according to ICG/NEAMTWS). The analysis focused on the magnitude of the 1980 earthquake (6.8), and the resulting alert levels from the DM for the stations are illustrated in Figure 4.18 a. Alert levels which derive from the simulations are shown in figure 4.18 b.

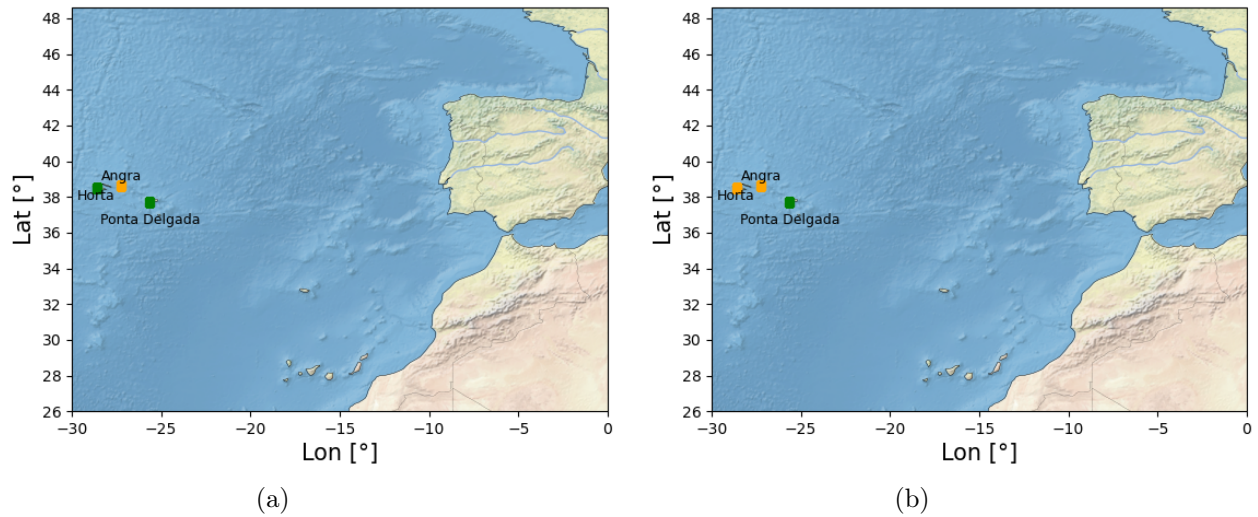


Figure 4.18: Comparison of expected alert levels for stations based on maximum wave heights resulting from simulations of the 1980 earthquake (magnitude 6.8), (a) strike-slip scenario, (b) dip-slip scenario. The alert levels (ICG/NEAMTWS) are determined by comparing the wave height values to the decision matrix (Table 2.5). In particular the choice of colors indicates: green=information, orange=advisory, red=watch, following the indication of table 2.3.

## 4.4 A dip-slip event: 28 February 1969

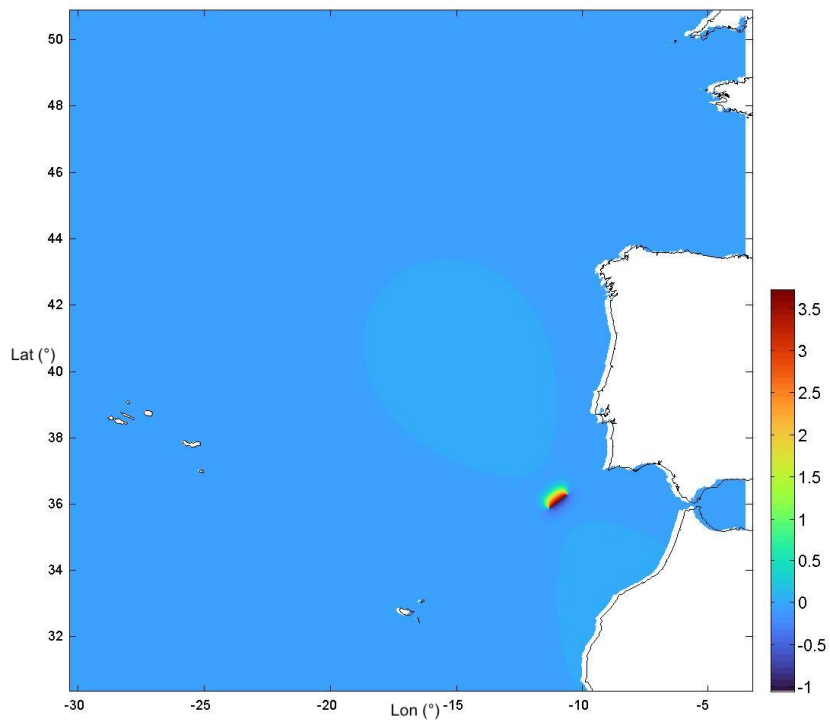
### 4.4.1 1969 dip-slip event

On the 28th February 1969, the coasts of Portugal, the Azores, Spain, Canary Islands, and Morocco were affected by a smaller tsunami generated by a submarine earthquake ( $M_s$  7.9; Table 2) with an epicenter located south of Gorringe bank ( $36.47^\circ N$ ,  $11.58^\circ W$ ) near the Azores-Gibraltar fracture zone (Fukao, 1973; Guesmia et al., 1998). This event is the most significant in terms of impact that occurred in the last century. The occurrence during the night at 02:40 reduced the number of eyewitness reports (Renou et al., 2011). The maximum amplitude of the tsunami is estimated to be 0.9 m at Casablanca, based on the tide gauge record of the harbor of Casablanca (Kaabouben et al., 2009). The Moroccan newspaper "Al Alam" from 1st and 2nd March 1969 reported the distressed behavior of people and strong sea agitation, mainly in Rabat and Sale, during the night. According to Baptista and Miranda (2009) as well as Omira et al. (2009) a dataset comprising a minimum of 13 tide records was obtained to determine the location of the tsunami source. The specific parameters associated with the tsunami source are presented in Table 4.14.

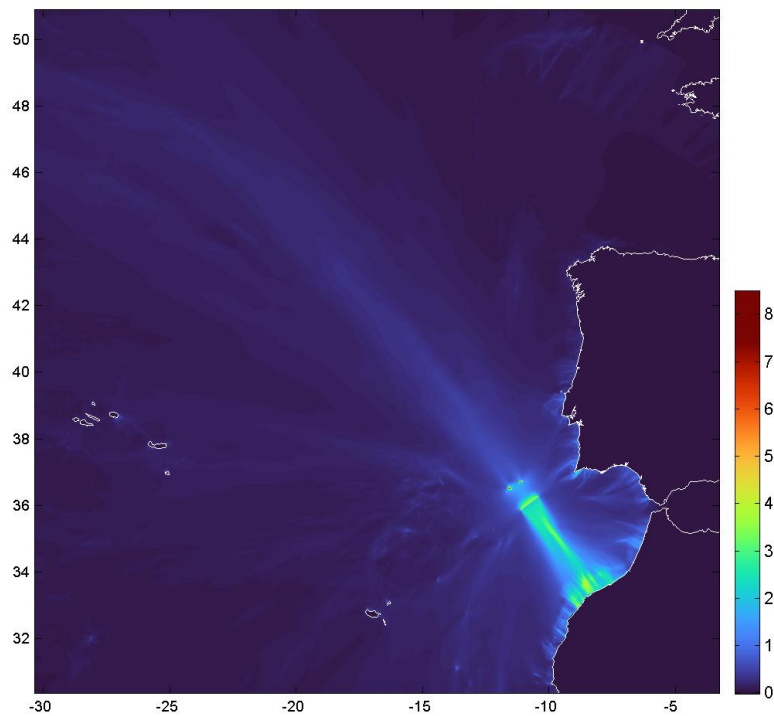
Scenario name	L (km)	W (km)	Epicenter coordinates		D (km)	slip (m)	Strike ( $^\circ$ )	Dip ( $^\circ$ )	Rake ( $^\circ$ )	$\mu$ (GPa)	$M_w$
			Lon	Lat							
1969	80	50	-10.57	36.01	22.0	3.0	235.0	52.0	90.0	40	7.9

Table 4.14: Source parameters (from Fukao, 1973), L: the fault length in kilometers; W: the fault width in kilometers; D: the depth from the sea bottom to the top of the fault in kilometers;  $\mu$ : the shear modulus and  $M_w$ : the moment magnitude.

Virtual stations have been simulated at the same locations as the 1941 event (Table



(a)



(b)

Figure 4.19: Tsunami numerical simulation for the 1969 dip-slip event. (a) The initial sea-surface perturbation (m) that follows the sea-bottom deformation. (b) The maximum tsunami wave heights (m) distribution.

4.15), allowing for a direct comparison between a strike-slip and dip-slip event.

Magnitude	Lon. and Lat. (°E , °N)	Max. amplitude (Dip) (m)
Ponta Delgada	-25.65, 37.73	0.34
Madeira	-16.91, 32.63	0.22
Leixões	-8.71, 41.17	0.30
Cascais	-9.41, 38.69	0.80
Casablanca	-7.59, 33.62	2.5
Essaouira	-9.78, 31.51	0.80
Lagos	-8.66, 37.10	1.05

Table 4.15: *POIs (points of interest) of the 1969 tsunami used in the Dip simulation, maximum amplitude associated.*

After simulating two scenarios, a real strike-slip and a dip-slip earthquake, the maximum wave heights were obtained and compared to the decision matrix (Table 2.5) to determine the appropriate alert level (watch, advisory, information, according to ICG/NEAMTWS). The analysis focused on the magnitude of the 1969 earthquake (7.9), and the resulting alert levels for the stations are illustrated in Figure 4.21 a. Alert levels which derive from the simulations are shown in figure 4.21 b.

## 4.5 Effects of Epicenter Displacement on Tsunami Impact

The accurate determination of earthquake epicenter location plays a crucial role in assessing the potential impact of tsunamis. In recent studies, the effects of epicenter relocation on tsunami impact have been investigated to better understand the significance of precise epicenter determination. By analyzing historical seismic events which

4.5. EFFECTS OF EPICENTER DISPLACEMENT ON TSUNAMI IMPACT 79

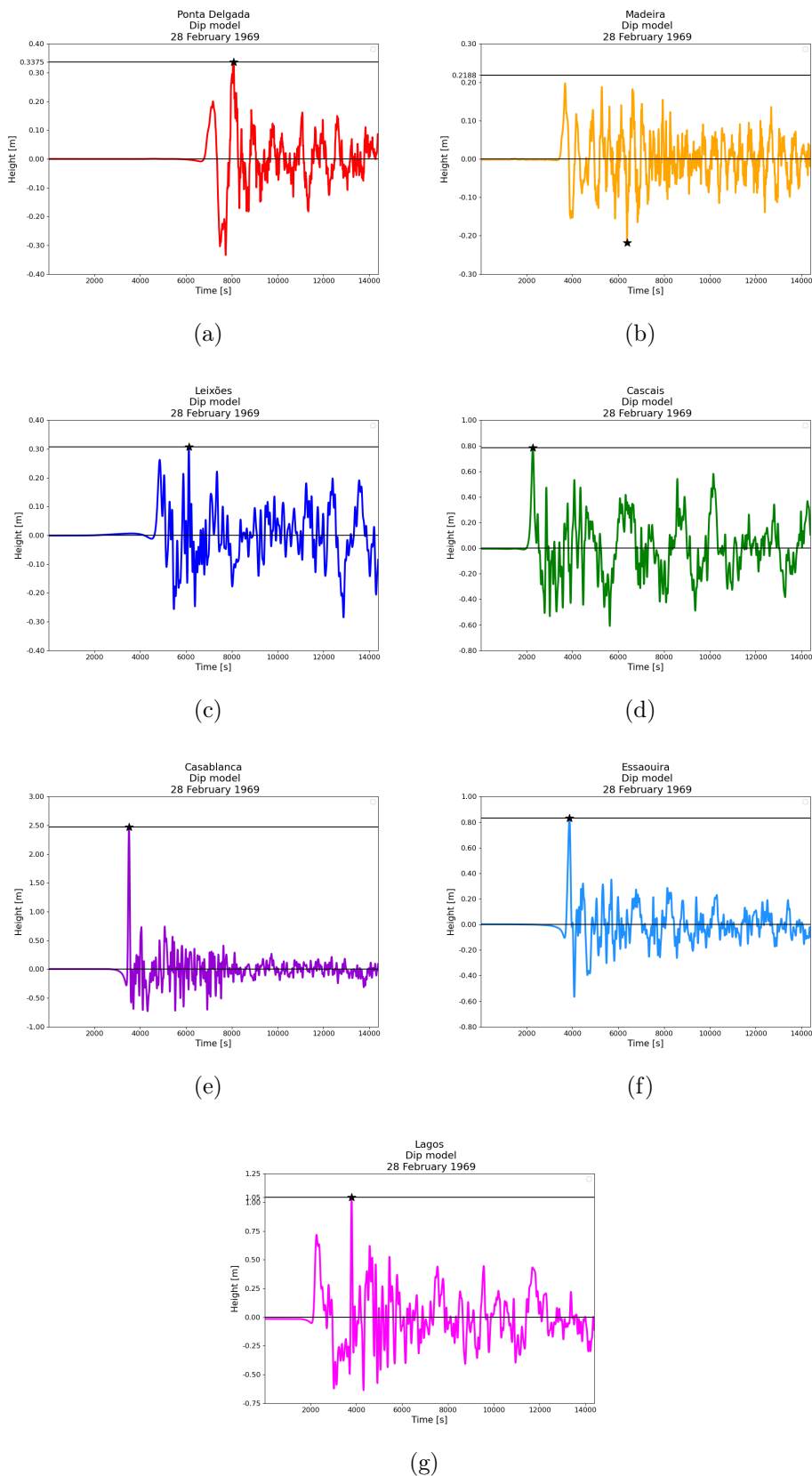


Figure 4.20: Modeled waveforms for the 1969 dip-slip event. (a-g) indicates in order the stations in table 4.15. The star denotes the highest amplitude of the modeled waveform, and its absolute value is represented by the solid black line.

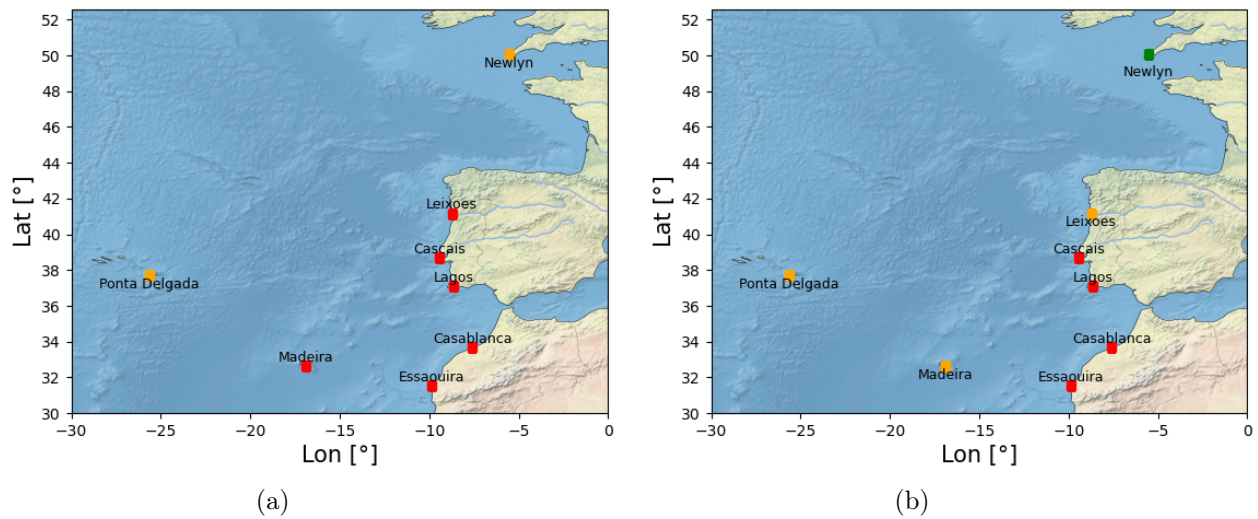


Figure 4.21: Comparison of expected alert levels for stations based on maximum wave heights resulting from simulations of the 1969 earthquake (magnitude 7.9). (a) The expected alert levels (ICG/NEAMTWS) are determined by comparing the wave height values to the decision matrix (Table 2.5). (b) Maximum wave heights resulting from simulations of the 1969 dip-slip scenario. In particular the choice of colors indicates: green=information, orange=advisory, red=watch, following the indication of table tab:Tinti.

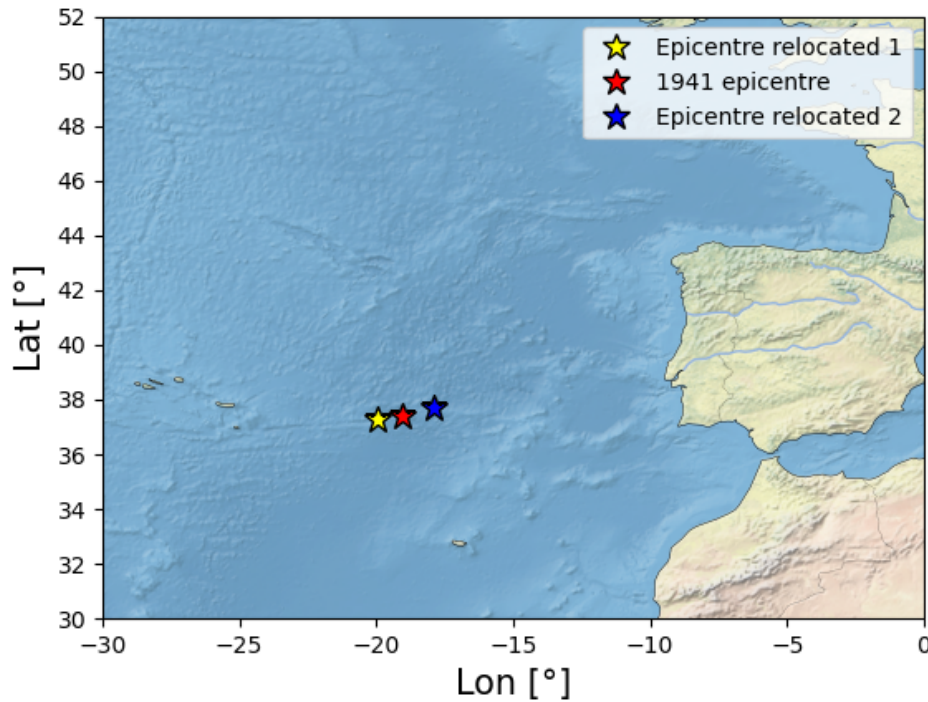


Figure 4.22: Location of the epicenters: case 1 of relocation in yellow, 1941 epicentre in red, and case 2 in blue.

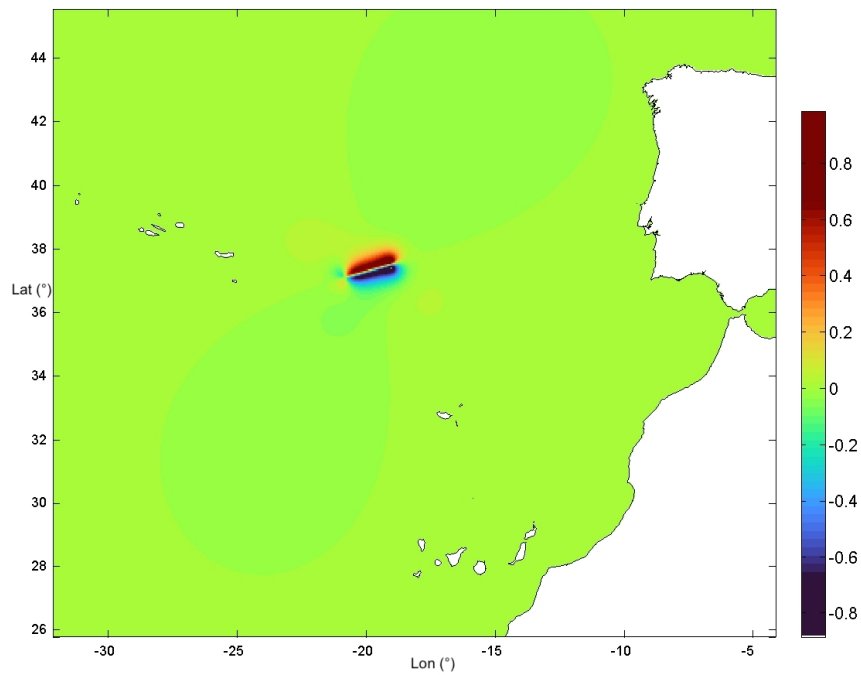
occurred in the vicinity of the Gloria Fault, the influence of epicenter relocation on tsunami characteristics and subsequent impact can be examined. In this paragraph, the focus will be shifted to the event of 1941 by relocating the epicenter in a north-east and then south-west direction, as illustrated in Figure 4.32. The new coordinates for the epicenter are provided in Table 4.16. Specifically, the selection of the new virtual epicenter locations is predicated on the source parameters of the 1941 event. Case 1 is positioned at the southwestern extremity, while Case 2 is situated at the northeastern endpoint of the 170 km fracture. As a result, the epicenter is displaced by a distance of 85 km in both cases. This change in location is intended to observe

Scenario name	L (km)	W (km)	Epicenter coordinates		D (km)	slip (m)	Strike (°)	Dip (°)	Rake (°)	$\mu$ (GPa)	$M_w$
			Lon	Lat							
1941	170	45	-19.04	37.41	54	8	254	88	161	45	8.3
Case 1	170	45	-19.95	37.25	54	8	254	88	161	45	8.3
Case 2	170	45	-17.92	37.72	54	8	254	88	161	45	8.3

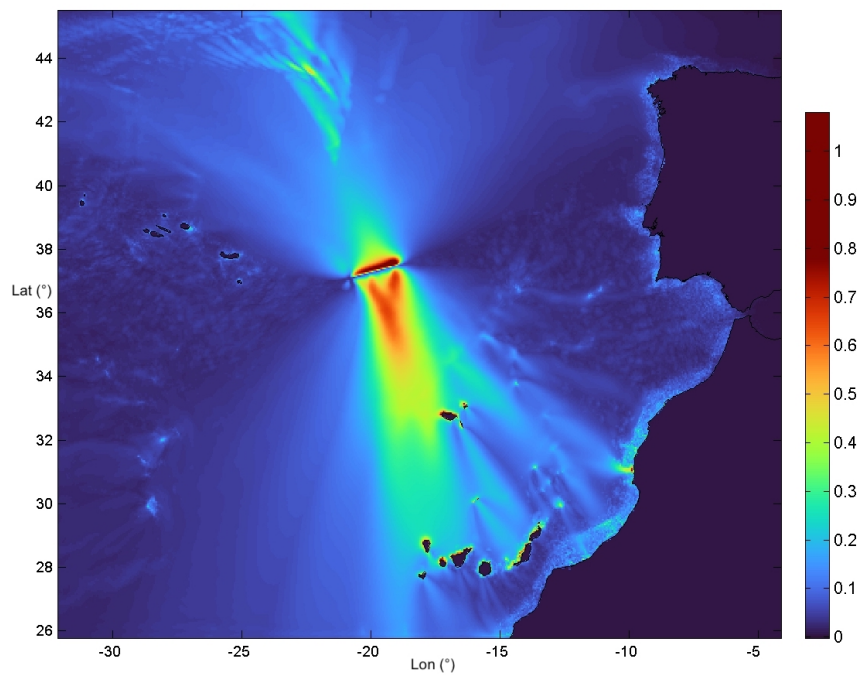
Table 4.16: Source parameters for the 1941 event (from Baptista, 2016) and for the two cases of relocation, L: the fault length in kilometers; W: the fault width in kilometers; D: the depth from the sea bottom to the top of the fault in kilometers;  $\mu$ : the shear modulus and  $M_w$ : the moment magnitude.

the resulting effects on wave heights. Through the process of relocating the epicenter, either by refining existing coordinates or exploring alternative locations, the resulting changes in parameters such as wave heights, arrival times, and inundation areas can be quantified. This research provides valuable insights into the sensitivity of tsunami impact to epicenter displacement and enhances our understanding of the complexities involved in tsunami hazard assessment. The findings contribute to the development of more accurate tsunami forecasting simulations and risk mitigation strategies, ultimately aiming to minimize the devastating consequences of these natural disasters. In addition, this investigation considers the effects of keeping the seismic stations fixed during the epicenter relocation process. By maintaining the station locations unchanged, the sole focus is on adjusting the epicenter coordinates. This approach allows for a more direct evaluation of the impact of epicenter relocation on tsunami characteristics, as it isolates the influence of station movement from the analysis. By comparing the results obtained from the original epicenter coordinates to those obtained after the relocation, any significant differences in wave heights, arrival times, or inundation areas can be attributed primarily to the relocation itself. This aspect

of the study provides valuable insights into the extent to which epicenter relocation affects the overall assessment of tsunami impact, shedding light on the importance of accurate epicenter determination for effective tsunami hazard evaluation. In Figure 4.25, the waveforms from two stations are shown. The reason for including only these waveforms is that these observations are not directly relevant to the modifications in the decision matrix. Empirical evidence demonstrates that the close proximity of the epicenter to a specific station leads to increased wave heights and earlier arrival times, aligning with our anticipated expectations. These observations hold true for any station, not limited to the two exemplified. From these findings, we can infer that altering the epicenter's position does not yield significant alterations in wave height or shape. The sole discernible effect is that proximity to certain stations results in larger wave amplitudes, while greater distance produces diminished wave magnitudes. In the specific case of the 1941 fracture (170 km), the alteration of the epicenter did not result in significant changes in the direction of the tsunami waves or their impact on coastal regions. The previous unaffected areas remained largely unaffected, and vulnerable areas did not experience a notable reduction in impact. Furthermore the relocation of the epicenter did not lead to a notable shift in the vulnerability of coastal regions. Areas that were previously considered low-risk did not become significantly more susceptible to tsunami impacts, nor did highly vulnerable regions experience a considerable decrease in risk. Finally changing the epicenter location did not necessitate substantial adjustments in tsunami warning systems and evacuation plans. The timing and magnitude of the tsunami were not significantly

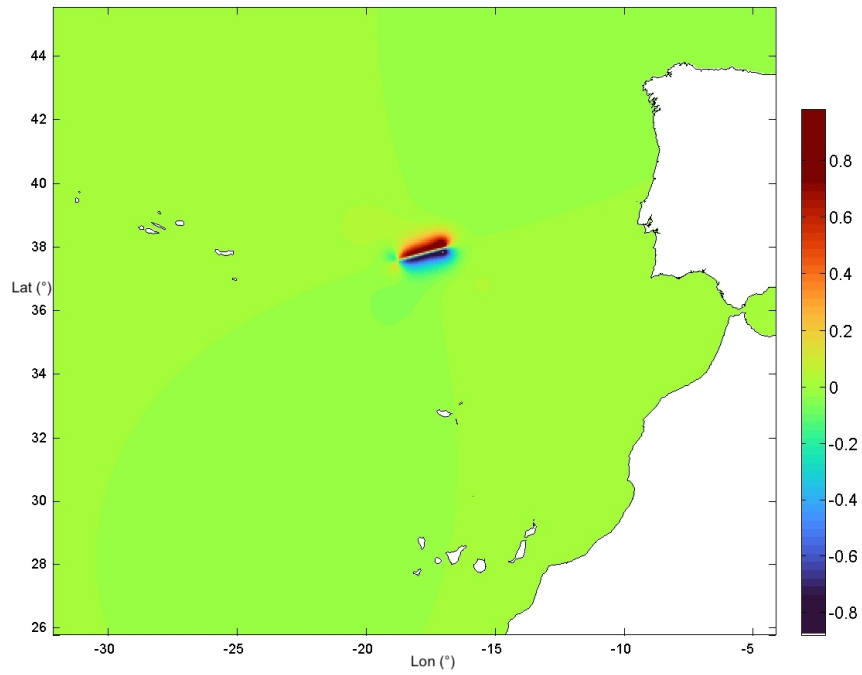


(a)

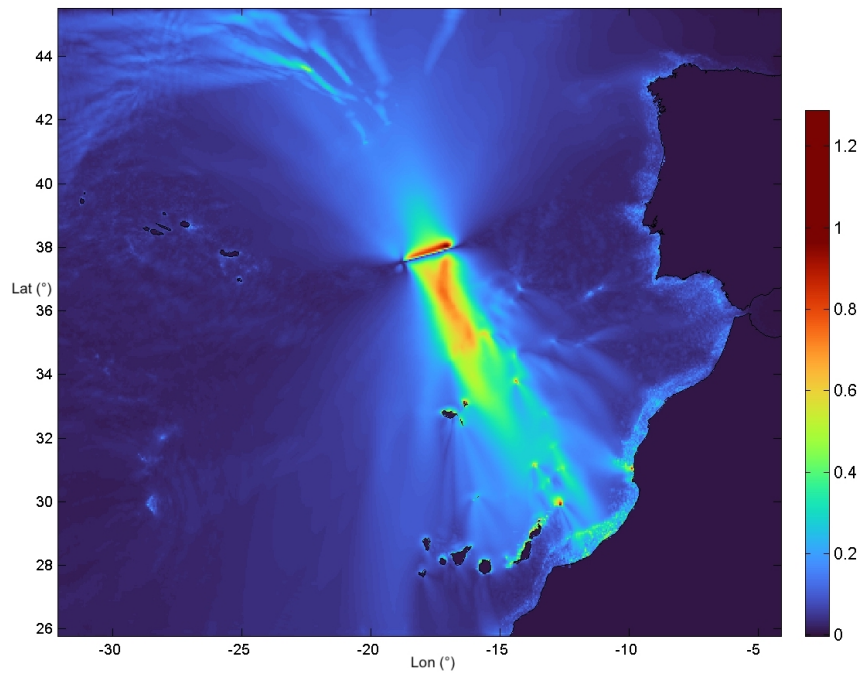


(b)

Figure 4.23: Tsunami numerical simulation for the 1941 relocated scenario (1). (a) The initial sea-surface perturbation (m) that follows the sea-bottom deformation. (b) The maximum tsunami wave heights (m) distribution.



(a)



(b)

Figure 4.24: Tsunami numerical simulation for the 1941 relocated scenario (2). (a) The initial sea-surface perturbation (m) that follows the sea-bottom deformation. (b) The maximum tsunami wave heights (m) distribution.

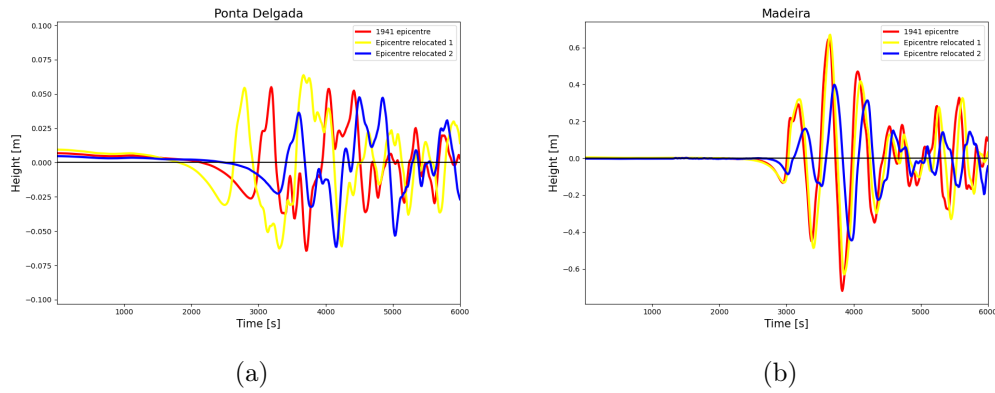


Figure 4.25: Modeled waveforms for the 1941 strike-slip event and the two relocated epicenters, in Ponta Delgada (a) and in Madeira (b).

affected by the relocation, thus not requiring extensive updates to alert systems or evacuation protocols. It is important to emphasize that these observations pertain specifically to the 1941 fracture (170 km) under consideration. Different tsunamis and fracture scenarios may exhibit different consequences when the epicenter location is changed, necessitating appropriate analysis and evaluation for each specific case to ensure the safety of coastal communities. In light of these considerations, the subsequent section, 4.6, has focused on investigating the potential effects resulting from modifications in magnitude. Such analyses are deemed to yield more intriguing results, given the aforementioned reasons.

## 4.6 Effects of Magnitude Modification on Tsunami Impact

The next step was to investigate the effects of magnitude modification on tsunami impact, with a particular emphasis on changing the slip component of the scenario. By altering the magnitude while keeping other parameters constant, such as the epicenter location and focal mechanism, the study aims to assess the significance of magnitude in determining tsunami characteristics. This analysis is crucial for the development of a new decision matrix or the modification of the existing one, as it provides insights into the relationship between magnitude and tsunami impact. By comparing the results obtained from scenarios with different magnitudes, specifically focusing on changes in wave heights, propagation patterns, and coastal inundation, the study seeks to identify the extent to which magnitude influences the overall assessment of tsunami hazard. These findings will contribute to the refinement of tsunami prediction methodologies and the formulation of more accurate and tailored decision matrices, taking into account the specific characteristics of the strike-slip behaviour of the GF. This study was done for the three strike-slip events presented before, 1941, 1975 and 1980 events. Keeping fixed the source parameters of table 4.1 for the 1941, table 4.6 for the 1975 and table 4.10 for the 1980, different magnitude events have been modeled, changing only the slip. The decision to modify solely the slip is associated with the fact that this parameter exhibits a more direct correlation with the initial wave height of the tsunami. For the 1941 the values are reported in table 4.17, for the 1975 the values are reported in table 4.18 and for the 1980 in

table 4.19.

1941 Event	
Magnitude	Slip
7.6	1
7.8	2
7.9	3
8.0	4
8.1	5
8.2	7
8.3	9
8.4	13

Table 4.17: Magnitudes and corresponding slip values for the 1941 event.

1975 Event	
Magnitude	Slip
7.6	3
7.8	6
7.9	11
8.0	12
8.1	17
8.2	24

Table 4.18: Magnitudes and corresponding slip values for the 1975 event.

1980 Event	
Magnitude	Slip
6.8	1
7.0	2
7.2	4
7.4	7
7.6	13
7.9	35
8.0	50
8.1	70

Table 4.19: Magnitudes and corresponding slip values for the 1980 event.

4.6. EFFECTS OF MAGNITUDE MODIFICATION ON TSUNAMI IMPACT 89

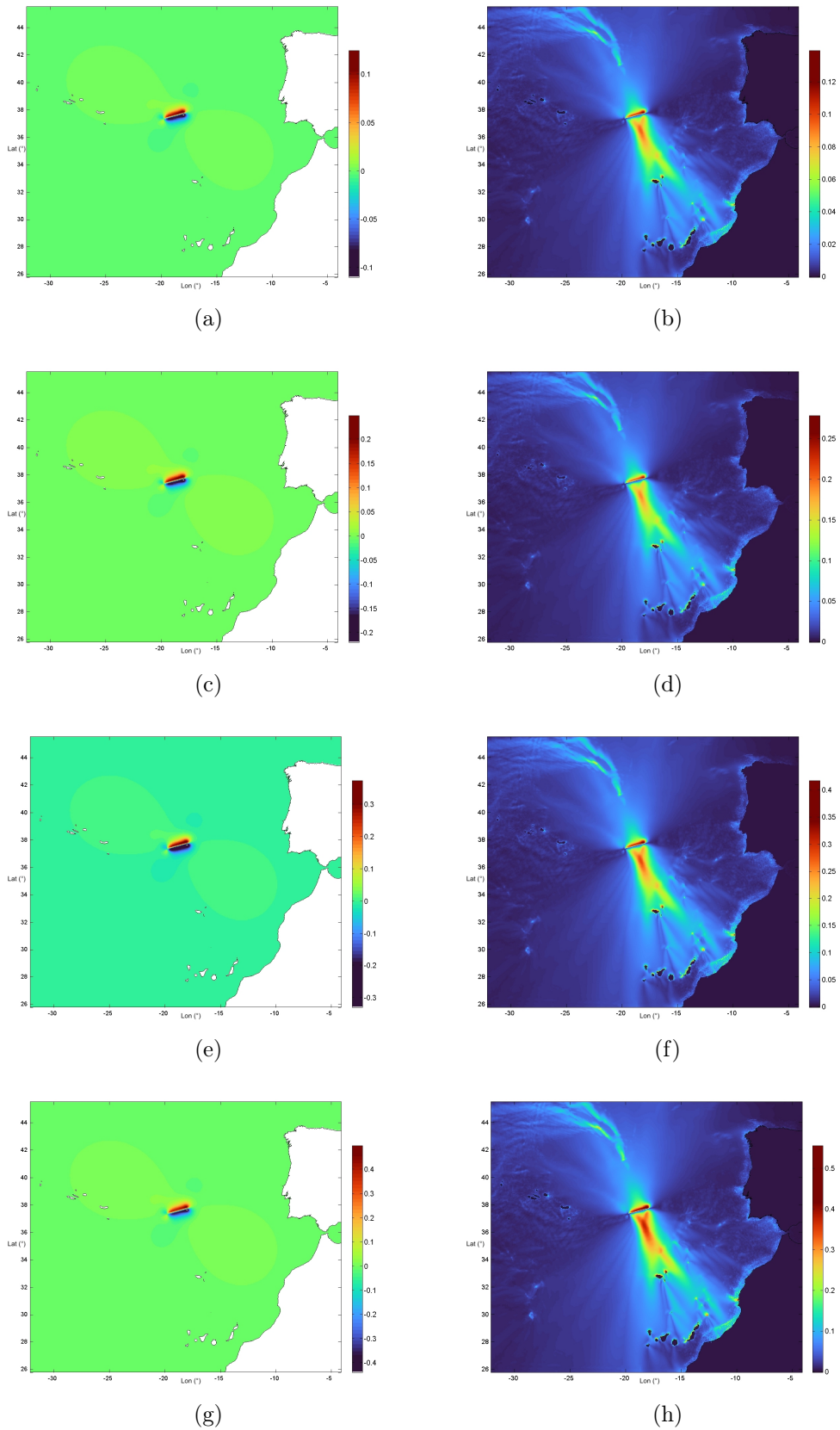


Figure 4.26: On the left: initial sea-surface perturbation (m) that follows the sea-bottom deformation with the 1941 source parameters. On the right: maximum tsunami wave heights distribution (m). In order of magnitudes  $M_w$ : 7.6 (a,b), 7.8 (c,d), 7.9 (e,f), 8.0 (g,h).

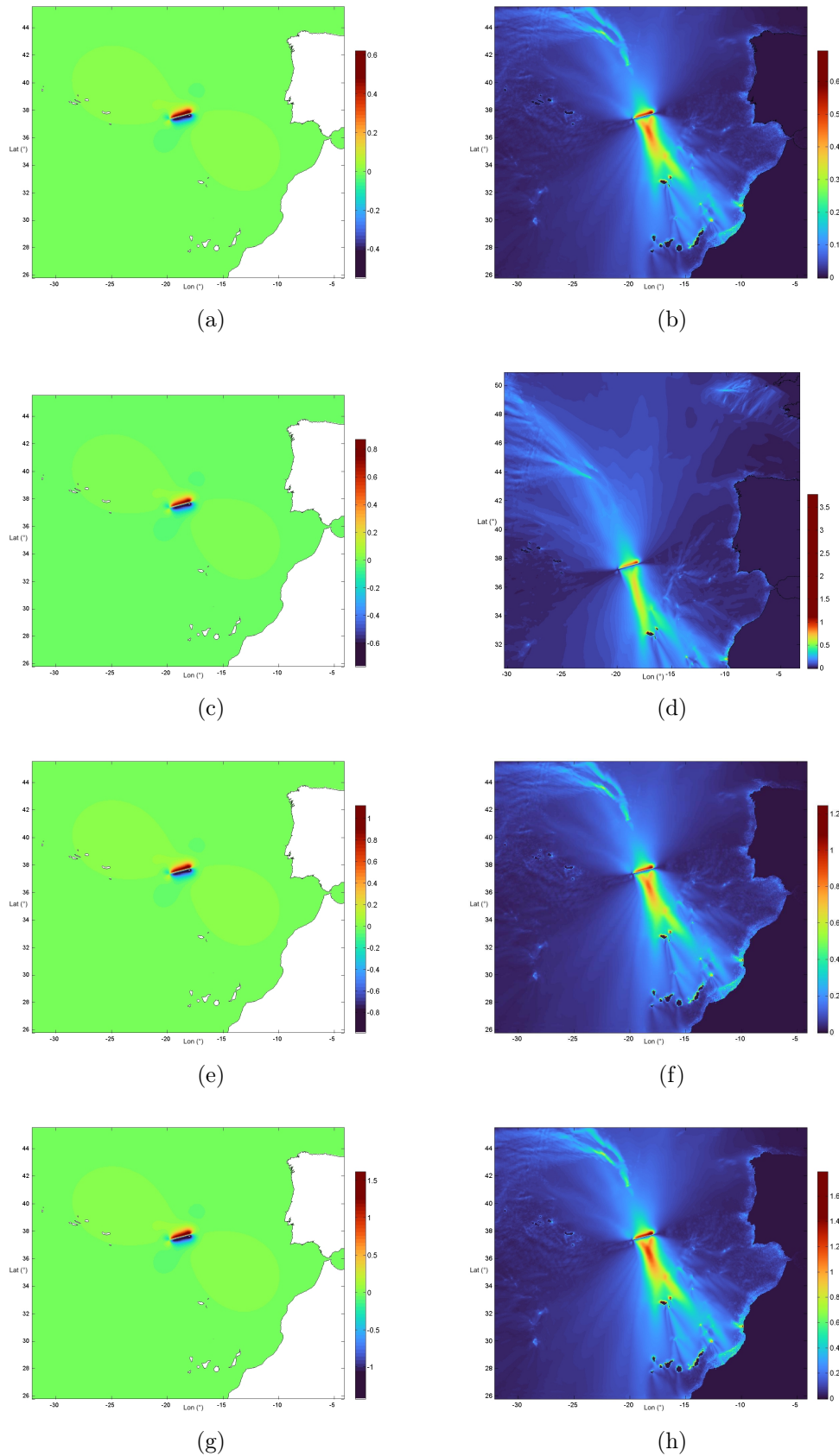


Figure 4.27: On the left: initial sea-surface perturbation (m) that follows the sea-bottom deformation with the 1941 source parameters. On the right: maximum tsunami wave heights distribution (m). In order of magnitudes  $M_w$ : 8.1 (a,b), 8.2 (c,d), 8.3 (e,f), 8.4 (g,h).

4.6. EFFECTS OF MAGNITUDE MODIFICATION ON TSUNAMI IMPACT 91

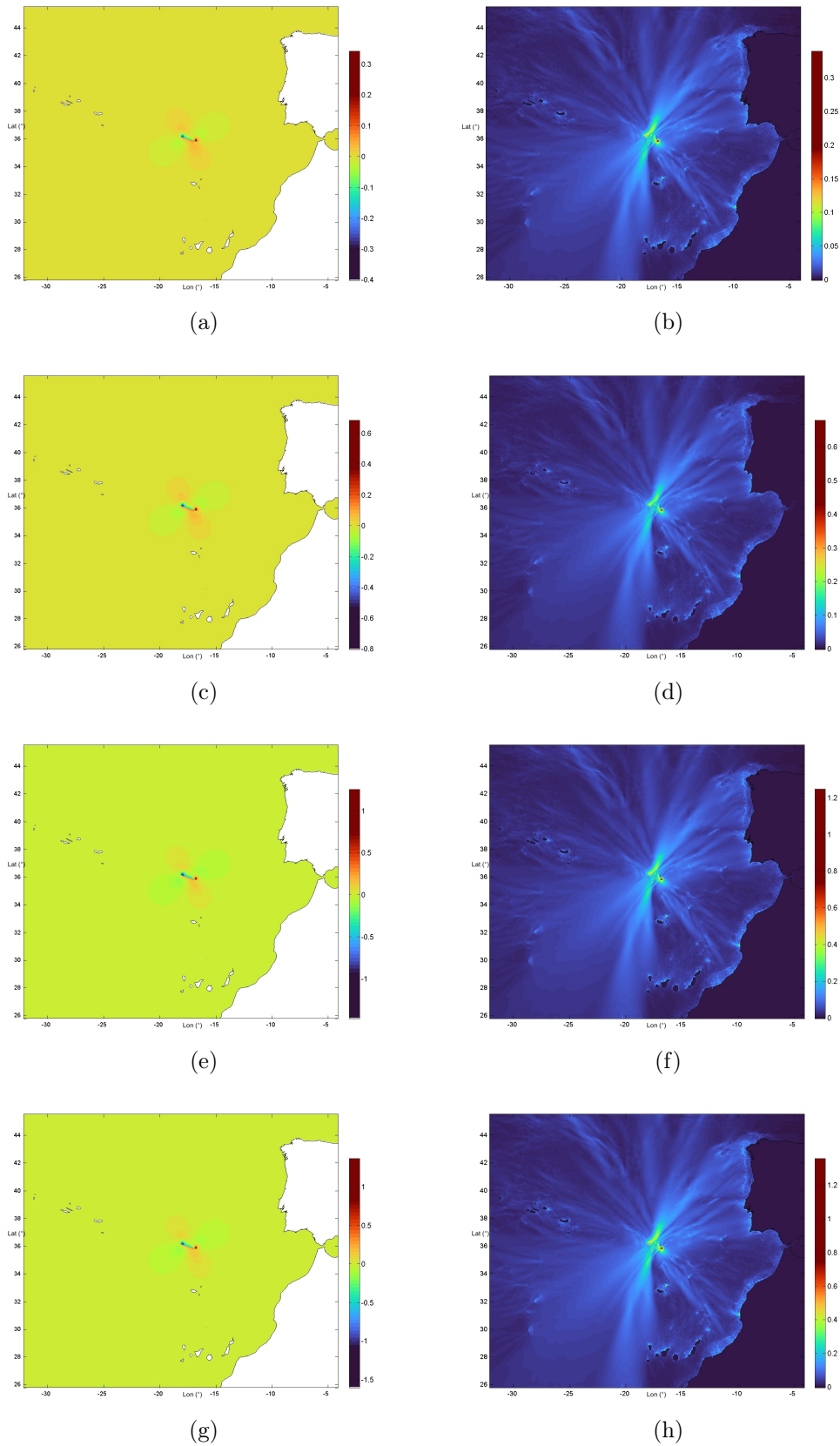


Figure 4.28: On the left: initial sea-surface perturbation (m) that follows the sea-bottom deformation with the 1975 source parameters. On the right: maximum tsunami wave heights distribution (m). In order of magnitudes  $M_w$ : 7.6 (a,b), 7.8 (c,d), 7.9 (e,f), 8.0 (g,h).

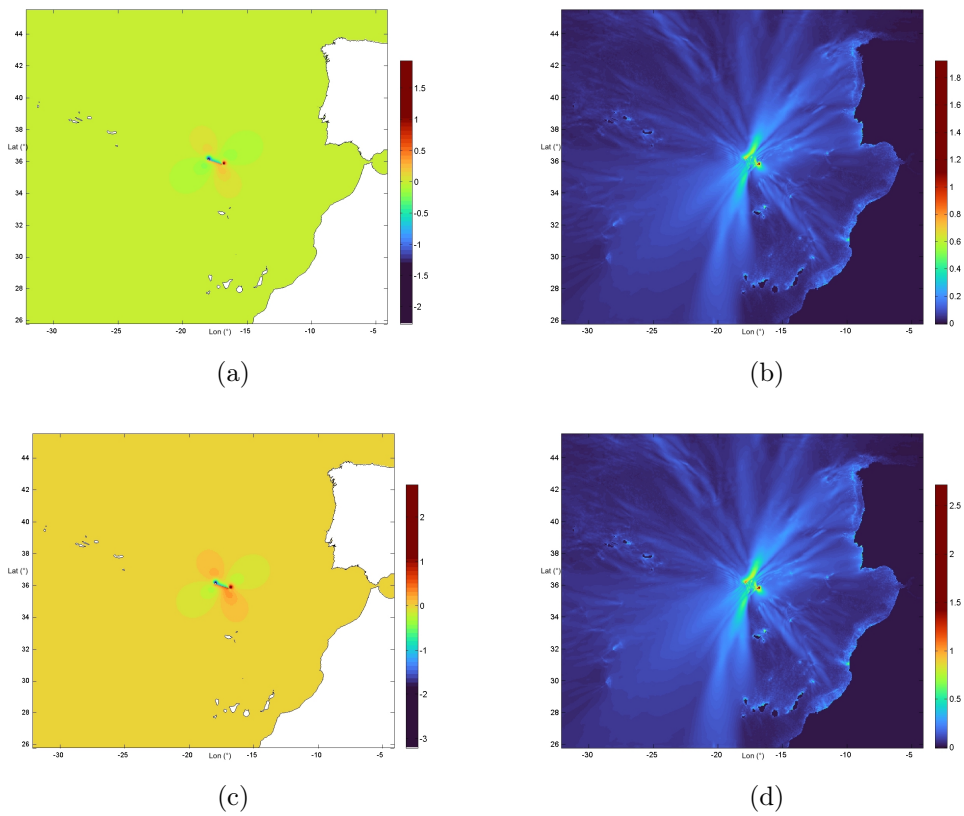


Figure 4.29: On the left: initial sea-surface perturbation (m) that follows the sea-bottom deformation with the 1975 source parameters. On the right: maximum tsunami wave heights distribution (m). In order of magnitudes  $M_w$ : 8.1 (a,b), 8.2 (c,d).

4.6. EFFECTS OF MAGNITUDE MODIFICATION ON TSUNAMI IMPACT 93

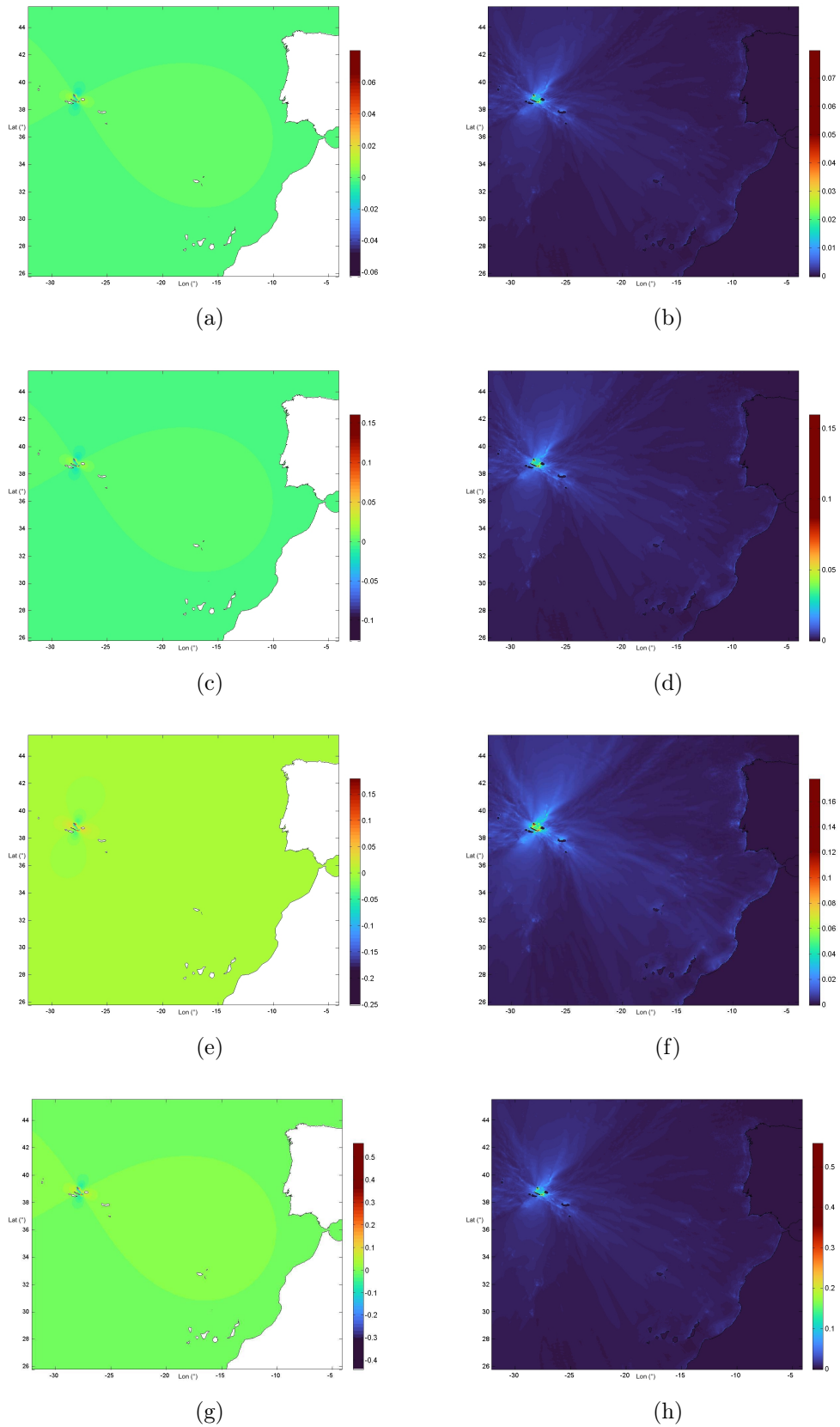


Figure 4.30: On the left: initial sea-surface perturbation (m) that follows the sea-bottom deformation with the 1980 source parameters. On the right: maximum tsunami wave heights distribution (m). In order of magnitudes  $M_w$ : 6.8 (a,b), 7.0 (c,d), 7.2 (e,f), 7.4(g,h)

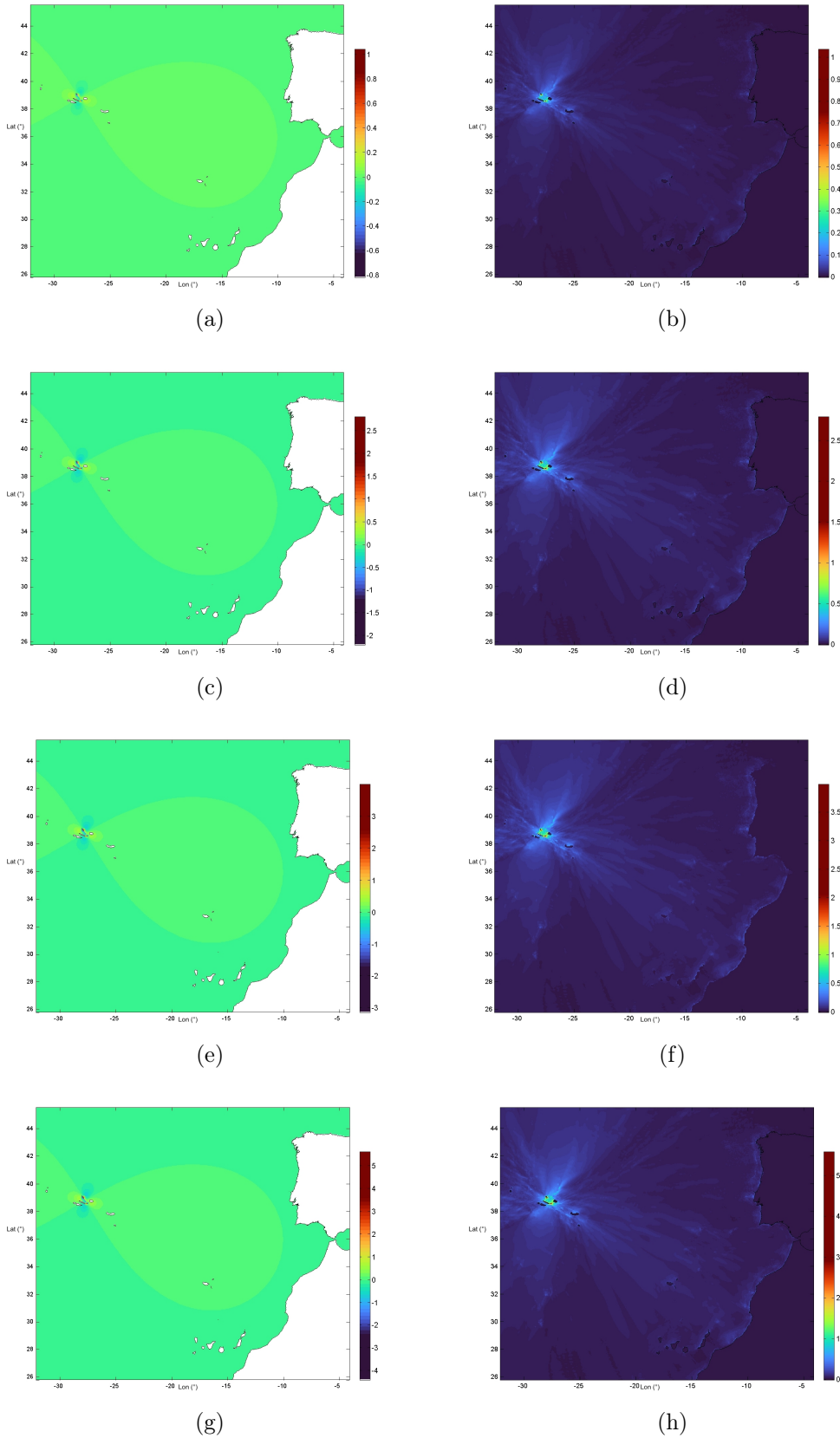


Figure 4.31: On the left: initial sea-surface perturbation (m) that follows the sea-bottom deformation with the 1980 source parameters. On the right: maximum tsunami wave heights distribution (m). In order of magnitudes  $M_w$ : 7.6 (a,b), 7.9 (c,d), 8.0 (e,f), 8.1 (g,h)

By conducting simulations encompassing a range of magnitudes and drawing upon the previous analysis of various events, it becomes possible to elucidate the distinct effects generated by tsunamis of different magnitudes along the Gloria Fault. Specifically, a comparison can be made between the results of the 1980 event, which occurred within a proximity of 40 km from the Azores, resulting in comparatively lower expected magnitudes, and the other two events, 1941 and 1975, which offer representations of higher magnitude events. In light of these considerations, the forthcoming section, 4.7, will introduce a new proposal DM for the North East Atlantic region.

## 4.7 New proposal for the DM in the NE Atlantic

Based on the findings presented in Section 4.6, specifically the maximum wave heights identified for each selected magnitude and scenario, it is feasible to develop a new decision matrix that aligns with the observed behavior of these events. This decision matrix incorporates distinct classifications based on proximity to the epicenter (tab. 2.4), including local distances ( $<100$  km), regional distances (between 100 km and 1000 km), and basin regions ( $>1000$  km). Specifically, considering various thresholds for information, advisory, and watch levels corresponding to the observed wave heights (tab. 2.3), an alert level has been established for each magnitude and event at different distances from the epicenter.

Upon reviewing these initial versions of the decision matrices, it is feasible to construct a new decision matrix (DM) by incorporating the 1980 DM, which pertains

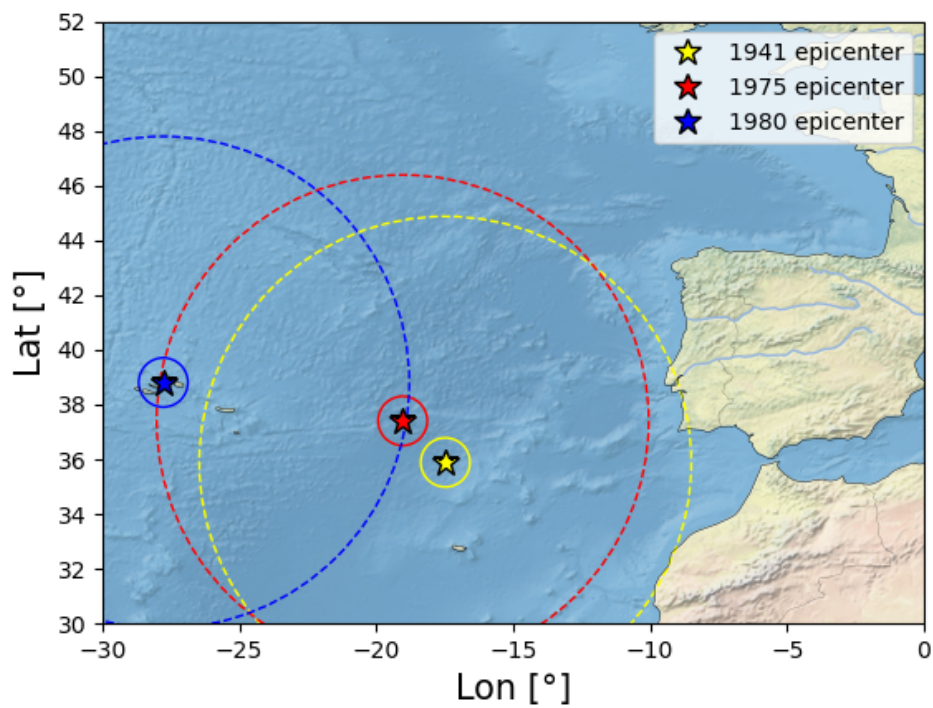


Figure 4.32: Location of the epicenters: 1941 epicentre in yellow, 1975 epicentre in red, and 1980 in blue. The circles represent the tsunami ranges: local inside the solid line, regional between solid and dashed lines, basin outside dashed line.

Event	Magnitude	Distance from Epicenter		
		Local	Regional	Basin
1941	7.6	I	I	I
	7.8	A	A	A
	7.9	A	A	A
	8.0	W	A	A
	8.1	W	W	A
	8.2	W	W	W
	8.3	W	W	W
	8.4	W	W	W

Table 4.20: Decision Matrix derived for the 1941 event.

Event	Magnitude	Distance from Epicenter		
		Local	Regional	Basin
1975	7.6	I	I	I
	7.8	W	I	I
	7.9	W	A	A
	8.0	W	A	A
	8.1	W	W	A
	8.2	W	W	A

Table 4.21: Decision Matrix derived for the 1975 event.

to events of lower magnitude occurring in proximity to the Azores coasts (within a distance of  $\leq 40km$ ), as well as the 1941 and 1975 DMs, which are relevant for offshore events of higher magnitudes. The resultant DM, derived from these three drafts, will adopt a highly cautious approach as it will consider any event surpassing the alert threshold across the entire region, without placing significant emphasis on wave height at specific stations.

Table 4.23 showcases the revised version of the DM (Decision Matrix) for the North-East Atlantic. By comparing this table with tab.2.5, notable adjustments can be observed. Specifically, the lower limit of the first alert level, indicating a weak potential for a destructive local tsunami, has been raised by 1.8 in magnitude units,

Event	Magnitude	Distance from Epicenter		
		Local	Regional	Basin
1980	6.8	I	I	I
	7.0	I	I	I
	7.2	I	I	I
	7.4	A	I	I
	7.6	A	I	I
	7.9	W	A	I
	8.0	W	A	A
	8.1	W	W	A

Table 4.22: Decision Matrix derived for the 1980 event.

while the upper limit has increased by 0.6. Although the magnitudes corresponding to the other alert levels show minimal changes, a significant reduction is evident in the range of magnitudes between a potential for a destructive local tsunami and an ocean-wide tsunami. Despite the expectation of an increase in the upper limit of the decision matrix, no such change was observed. In conclusion, for a strike-slip fault system, it can be inferred that earthquakes below a magnitude of 7.4 do not generate destructive tsunamis.

DM for the NE Atlantic						
Depth (km)	Epicenter Location	Earthquake Magnitude ( $M_w$ )	Tsunami Potential	Type of Tsunami Message		
				Local	Regional	Basin
<100 km	Offshore or close to the coast ( $\leq 40$ km)	$>7.3$ and $\leq 7.6$	Weak potential for a destructive local Tsunami	A	I	I
	Offshore or close to the coast ( $\leq 100$ km)	$>7.7$ and $\leq 8.0$	Potential for a destructive local Tsunami	W	A	I
		$>8.0$ and $\leq 8.1$	Potential for a destructive regional Tsunami	W	W	A
		$>8.2$	Potential for a destructive ocean-wide Tsunami	W	W	W

Table 4.23: New proposal of the Decision Matrix for the North East Atlantic.



## Chapter 5

# Conclusions

This thesis examines the occurrences of tsunamis in the Tsunamigenic Zone of the Gloria Fault in the North East Atlantic. The primary objective of this research is to investigate whether the tsunamis that occurred in the 20th century align with the predicted alerts provided by the decision matrix for North East Atlantic (Tab. 2.5), and to develop an enhanced decision matrix specifically tailored for strike-slip events in this region.

The investigation of 20th century events along the Gloria Fault involved the utilization of the Mirone software, which incorporated the focal mechanisms of the examined tsunamis. This approach enabled the simulation of tsunamis in the region under study.

Chapter 4 of the study focused on analyzing the events that occurred on 25th November 1941, 28th February 1969, 26th May 1975, and 1st January 1980. The analysis reveals that for each of the three strike-slip events considered, the decision matrix

issued a higher alert, whereas the respective dip-slip scenario and the 1969 dip-slip event exhibited better consistency with the decision matrix alert. Subsequently, in the final section of the chapter, *New proposal for the DM in the NE Atlantic*, the thesis proceeds to construct a novel decision matrix based on modeled wave heights derived from these events (Tab. 4.17, 4.18 and 4.19). This approach, although highly conservative as it identifies the maximum wave height across different regions (local, regional, basin) rather than at a specific monitoring station, yields an improved matrix (Tab. 4.20) that enhances the alert levels in this particular region. Notably, it raises the lower limit of the alert, which aligns with the adopted decision matrix for the North East Atlantic region, particularly at higher alert values. In order to augment the present research, several potential enhancements can be considered. Firstly, refining the definition of local, regional, and basin regions would be beneficial. Specifically, tsunamis with magnitudes surpassing 8.2 exhibit the potential for substantial destruction in the broader basin region, which includes the coasts of Portugal and Morocco, while having minimal impact on the northern European coast. By delineating these regions more precisely, a more accurate assessment of the tsunami's impact on different areas can be obtained.

Furthermore, expanding the scope of the simulations to encompass the entire Gloria Fault, rather than solely focusing on the most significant events, would represent a notable improvement. By simulating tsunamis along the entire fault line, a comprehensive understanding of the potential tsunami scenarios can be achieved. This expanded simulation approach would provide insights into the behavior and charac-

teristics of tsunamis originating from various points along the fault, contributing to a more comprehensive analysis.

These improvements would strengthen the research outcomes by refining the spatial analysis of tsunamis and incorporating a broader range of potential events. The refined definition of regions and the comprehensive simulation approach would yield a more accurate assessment of tsunami hazards and contribute to the development of effective mitigation strategies in the North East Atlantic region.







# Bibliography

- [1] Aki, K. (1972). Earthquake mechanism. *Tectonophysics*, 13(1-4), 423-446.
  
- [2] Baptista M.A., Miranda P.M., Victor L.M. (1992) Maximum entropy analysis of Portuguese tsunami data. The tsunamis of 28.02.1969 and 26.05.1975. *Sci Tsunami Hazards* 10. 9–20.
  
- [3] Baptista, M.A., Miranda, J.M. (2009). Revision of the Portuguese catalog of tsunamis. *Nat. Hazards Earth Syst. Sci.*, 9, 25–42.
  
- [4] Baptista, M.A., Miranda, J.M., Matias, L., Omira, R. (2009). Synthetic tsunami waveform catalogs with kinematic constraints. *Nat. Hazards Earth Syst. Sci.*, 17 (7), 1253.
  
- [5] Baptista, M.A., Omira, R., Matias, L., Miranda, J.M., Catita, C., Carrilho, F., Toto, E. (2009). Design of a Sea-level Tsunami Detection Network for the Gulf of Cadiz. *Nat. Hazards Earth Syst. Sci.*, 9, 1327–1338.
  
- [6] Baptista, M. A., Miranda, J. M., Batlló, J., Lisboa, F., Luis, J., Macia, R. (2016). New study on the 1941 Gloria Fault earthquake and tsunami. *Natural*

- Hazards and Earth System Sciences, 16(8), 1967–1977.
- [7] Batista, L., Hübscher, C., Terrinha, P., Matias, L., Afilhado, A., Lüdmann, T. (2017). Crustal structure of the Eurasia– Africa plate boundary across the Gloria Fault, North Atlantic Ocean. *Geophys. J. Int.*, 209, 713–729.
- [8] Borges, J.F., Bezzeghoud, M., Buforn, E., Pro, C., Fitas, A. (2007). The 1980, 1997 and 1998 Azores earthquakes and some seismotectonic implications. *Tectonophysics*, 435 (2007), 37–54.
- [9] Buforn, E., Jimenez, M.J., Udías, A. (1983). Parámetros focales de los terremotos de 26 de Mayo de 1975 y 1 de Enero de 1980 en la región de Azores–Gibraltar y sismotectónica regional. *Rev. Geofis.*, 39, 51–63.
- [10] Buforn, E., Udías, A., Colombás, M.A. (1988). Seismicity, source mechanisms and seismotectonics of the Azores–Gibraltar plate boundary. *Tectonophysics*, 152, 89–118.
- [11] Buforn, E., Udías, A., Colombás, M.A. (1988). Seismicity source of the mechanisms and tectonics of the Azores- Gibraltar plate boundary. *Tectonophysics*, 152, 89–118.
- [12] Custódio, S., Lima, V., Vales, D., Cesca, S., Carrilho, F., 2016. Imaging active faulting in a region of distributed deformation from the joint clustering of focal mechanisms and hypocentres: application to the Azores–western Mediterranean region. *Tectonophysics* 676, 70–89.

- [13] Debrach, J. (1946). Raz de mareée d'origine sismique enregistré sur le littoral atlantique du Maroc (in French). *Annales, Maroc: Service de Physique du Globe et de l'institut scientifique Chérifien*.
- [14] Di Filippo, D. (1949). Il terremoto delle Azzore del 25 Nov. 1941. *Annali Geofis*, 2, 400–405.
- [15] Dutykh, D., Dias, F. (2007) Water waves generated by a moving bottom. In *Tsunami and Non- linear waves* (pp. 65-95), Springer Berlin Heidelberg
- [16] Fukao, Y. (1973). Thrust faulting at a lithospheric plate boundary, the Portugal earthquake of 1969. *Earth Planet Sc. Lett.*, 18, 205–216.
- [17] Grimison, N., Chen, W. (1988). The Azores–Gibraltar plate boundary: focal mechanisms, depths of earthquakes and their tectonic implications. *J. Geophys. Res.*, 91, 2029–2047.
- [18] Guesmia, M., Heinrich, P.H., Mariotti, C. (1998). Numerical simulation of the 1969 Portuguese tsunami by a finite element method. *Nat. Hazards*, 17, 31–46.
- [19] Hirn, A., Haessler, J., Hoang Trong, P., Wittlinger, G., Mendes Victor, L. (1980). Aftershock sequence of the January 1st, 1980 earthquake and present-day tectonics in the Azores. *Geophys. Res. Lett.*, 7, 501–504.
- [20] Imamura, F. (1995). Long waves in two-layers: governing equations and numerical model. *Sci. Tsunami Hazards*, 13(1), 3–24.

- [21] Kaabouben, F., Iben Brahim, A., Toto, E., Baptista, M.A., Miranda, J.M., Soares, P., Luis, J.F. (2007). On the focal mechanism of the 26.05.1975 North Atlantic event contribution from tsunami modeling.
- [22] Kaabouben, F., Brahim, A.I., Toto, E. et al. On the focal mechanism of the 26.05.1975 North Atlantic event contribution from tsunami modeling. *J Seismol* 12, 575–583 (2008). <https://doi.org/10.1007/s10950-008-9110-6>
- [23] Kaabouben, F., Baptista, M.A., Iben Brahim, A., El Mouraouah, A., Toto, A. (2009). On the moroccan tsunami catalogue. *Nat. Hazards Earth Syst. Sci.*, 9, 1227–1236.
- [24] Kajiura, K. (1970): Tsunami source, energy and the directivity of wave radiation. *Bull. Earthq. Res. Inst.*, 48, 835–869.
- [25] Kanamori, H., Anderson, D.L. (1977). Importance of physical dispersion in surface-wave and free oscillation problems – review. *Rev. Geophys.*, 15(1), 105–112.
- [26] Linsley, R.K., Franzini, J.B. (1979) *Water Resources Engineering*. 3rd Edition. McGraw-Hill Book Co., New York, pp 125–126
- [27] Liu, P. L.-F., Woo, S.-B., and Cho, Y.-S.: Computer programs for tsunami propagation and inundation, Technical report, Cornell University, 1998.
- [28] Lorito, S., Tiberti, M. M., Basili, R., Piatanesi, A., and Valensise, G. (2008), Earthquake-generated tsunamis in the Mediterranean Sea: Scenar-

- ios of potential threats to Southern Italy, *J. Geophys. Res.*, 113, B01301, doi:10.1029/2007JB004943.
- [29] Lorito, S., Tiberti, M.M., Basili, R., Piatanesi, A., Valensise, G. (2011). Earthquake-generated tsunamis in the Mediterranean Sea: Scenarios of potential threats to Southern Italy.
- [30] Luis, J., Mirone: A multi-purpose tool for exploring grid data, January 2007, *Computers Geosciences*, 33(1), 31-41.
- [31] Lynnes CS, Ruff LJ (1985) Source process and tectonic implications of the great 1975 North Atlantic earthquake. *Geophys J R Astron Soc* 82:497–510
- [32] Machado, F., Silveira, E., 1982. O terremoto de 1 Jan. 1980 e a tectónicas dos Açores. *Açoreana* 6, 155–170.
- [33] Mansinha, L., Smylie, D.E. (1971). The Displacements Fields of Inclined Faults. *Bulletin of the Seismological Society of America*, 61, 1433-1440.
- [34] Miranda, J.M., Luis, J.F., Reis, C., Omira, R., Baptista, M.A. (2014). Validation of NSWING, a multicore finite difference code for tsunami propagation and run-up. Paper Number S21A-4390, Natural hazards, American geophysical union (AGU) fall meeting, San Francisco.
- [35] Moreira, V. S. (1968). Tsunamis observados em Portugal. *Publicacao GEO*, 134 (in Portuguese).

- [36] Moreira, V.S. (1985). Seismotectonics of Portugal and its adjacent area in the Atlantic. *Tectonophysics*, 117, 85–96.
- [37] Nakanishi, I., Kanamori, H. (1984). Source mechanisms of twenty-six large, shallow earthquakes ( $M_s = 6.5$ ) during 1980 from P-wave first motion and long-period Rayleigh wave data. *Bull. Seismol. Soc. Am.*, 74, 805–818.
- [38] Neres, M., Carafa, M.M.C., Fernandes, R.M.S., Matias, L., Duarte, J.C., Barba, S., Terrinha, P. (2016). Lithospheric deformation in the Africa-Iberia plate boundary: improved neotectonic modeling testing a basal-driven Alboran plate. *J. Geophys. Res. Solid Earth*, 121, 6566–6596.
- [39] Okada, Y. (1985). Surface deformation due to shear and tensile faults in a half-space. *Bulletin of the Seismological Society of America*, 75(4), 1135–1154.
- [40] Omira, R., Baptista, M.A., Matias, L., Miranda, J.M., Catita, C., Carrilho, F., Toto, E. (2009). Design of a Sea-level Tsunami Detection Network for the Gulf of Cadiz. *Nat. Hazards Earth Syst. Sci.*, 9, 1327–1338.
- [41] Omira, R., Baptista, M.A., Iben Brahim, A., El Mouraouah, A., Toto, A. (2009). On the Moroccan tsunami catalogue. *Nat. Hazards Earth Syst. Sci.*, 9, 1227–1236.
- [42] Omira, R. (2010) Modeling Tsunamis Impact in northwestern Morocco and southwestern Iberia. PhD-Dissertation, Ibn Tofail University, Morocco

- [43] Omira, R., Neres, M., Batista, L. (2019). The Gloria Transform Fault—NE Atlantic: Seismogenic and Tsunamigenic Potential. 10.1016/B978-0-12-812064-4.00008-6.
- [44] Okada, Y. (1985). Surface Deformation Due to Shear and Tensile Faults in a Half-Space, *Bulletin of the Seismological Society of America*, 75, 4, 1135-1154.
- [45] Renou, C., Lesne, O., Mangin, A., Rouffi, F., Atillah, A., El Hadani, D., Moudni, H. (2011). Tsunami hazard assessment in the coastal area of Rabat and Salé, Morocco.
- [46] Synolakis, C.E., Bernard, E.N. (2006) Tsunami science before and beyond Boxing Day 2004. *Phil. Trans. R. Soc. A*.3642231–2265, <http://doi.org/10.1098/rsta.2006.1824>
- [47] Tanioka, Y., Satake, K., (1996). Tsunami generation by horizontal displacement of ocean bottom. *Geophysical Research Letters - GEOPHYS RES LETT*. 23. 861-864. 10.1029/96GL00736.
- [48] Tinti, S., Pagnoni, G., Maramai, A., Manucci, A., Tonini, R. (2008). Development of a New Tsunami Scenario Database for the Mediterranean Basin.
- [49] Tinti, S., Graziani, L., Brizuela, B., Maramai, A., Gallazzi, S. (2012). Applicability of the Decision Matrix of North Eastern Atlantic, Mediterranean and connected seas Tsunami Warning System to the Italian tsunamis. *Natural Hazards and Earth System Sciences*, 12, 843-857. DOI: 10.5194/nhess-12-843-2012.

- [50] Tinti, S., Tonini, R. (2013) The UBO-TSUFDF tsunami inundation model: validation and application to a tsunami case study focused on the city of Catania. Italy. *Nat. Hazards Earth Syst. Sci.* 13(7):1795–1816. <https://doi.org/10.5194/nhess-13-1795-2013>
- [51] Titov, V.V., Synolakis, C.E. (1995) Modeling of breaking and nonbreaking long-wave evolution and runup using VTCS-2. *J. Waterway Port Ocean Coast. Eng.* 121(6):308–316, [https://doi.org/10.1061/\(ASCE\)0733-950X\(1995\)121:6\(308\)](https://doi.org/10.1061/(ASCE)0733-950X(1995)121:6(308))
- [52] Titov, V.V., Synolakis, C.E. (1998) Numerical modeling of tidal wave runup. *J. Waterway Port Ocean Coast. Eng.* 124: 157–171
- [53] Tonini, R., Armigliato, A., Pagnoni, G., Zaniboni, F., Tinti, S. (2011) Tsunami hazard for the city of Catania, eastern Sicily, Italy, assessed by means of Worst-case Credible Tsunami Scenario Analysis (WCTSA). *Nat. Hazards Earth Syst. Sci.* 11(5), 1217-1232
- [54] Turcotte, D.L., Schubert, G., *Geodynamics*, (2014).
- [55] Udias, A., Arroyo, A. L., Mezcuca, J. (1976). Seismotectonic of the Azores-Alboran region. *Tectonophysics*, 31(3–4), 259–289.
- [56] Wronna M., *Tsunamis from source to coast*, PhD Thesis, 2021.
- [57] Yahav, A., Salamon, A. (2022). Tsunami Alert Efficiency. *Encyclopedia*, 2, 383–399.